Aerodynamic Models for the Low Density Supersonic Decelerator (LDSD) Test Vehicles

John W. Van Norman[1]
Analytical Mechanics Associates, Hampton, Virginia, 23666

Artem Dyakonov[2], Mark Schoenenberger[3], and Jody Davis[4]
NASA Langley Research Center, Hampton, Virginia, 23681

Suman Muppidi[5]
Analytical Mechanics Associates, Hampton, Virginia, 23666

Chun Tang[6] and Deepak Bose[7]
NASA Ames Research Center, Mountain View, California, 94035

Brandon Mobley[8]
Marshall Space Flight Center, Huntsville, Alabama, 35811

Ian Clark[9]
Jet Propulsion Laboratory, Pasadena, California, 91109

An overview of aerodynamic models for the Low Density Supersonic Decelerator (LDSD) Supersonic Flight Dynamics Test (SFDT) campaign test vehicle is presented, with comparisons to reconstructed flight data and discussion of model updates. The SFDT campaign objective is to test Supersonic Inflatable Aerodynamic Decelerator (SIAD) and large supersonic parachute technologies at high altitude Earth conditions relevant to entry, descent, and landing (EDL) at Mars. Nominal SIAD test conditions are attained by lifting a test vehicle (TV) to 36 km altitude with a helium balloon, then accelerating the TV to Mach 4 and 53 km altitude with a solid rocket motor. Test flights conducted in June of 2014 (SFDT-1) and 2015 (SFDT-2) each successfully delivered a 6 meter diameter decelerator (SIAD-R) to test conditions and several seconds of flight, and were successful in demonstrating the SFDT flight system concept and SIAD-R technology. Aerodynamic models and uncertainties developed for the SFDT campaign are presented, including the methods used to generate them and their implementation within an aerodynamic database (ADB) routine for flight simulations. Pre- and post-flight aerodynamic models are compared against reconstructed flight data and model changes based upon knowledge gained from the flights are discussed. The pre-flight powered phase model is shown to have a significant contribution to off-nominal SFDT trajectory lofting, while coast and SIAD phase models behaved much as predicted.

[1] Senior Project Engineer, AIAA Member
[2] Aerospace Engineer, Atmospheric Flight and Entry Systems Branch, AIAA Member
[3] Aerospace Engineer, Atmospheric Flight and Entry Systems Branch, AIAA Member
[4] Aerospace Engineer, Atmospheric Flight and Entry Systems Branch, AIAA Member
[5] Research Scientist, AIAA Senior Member
[6] Research Scientist, AIAA Senior Member
[7] Aerospace Engineer, AIAA Associate Fellow
[8] Aerospace Engineer, AIAA Member
[9] LDSD Pricipal Investigator, AIAA Member

Nomenclature

A_{ref}	=	reference area
ADB	=	aerodynamic database
BCS	=	body coordinate system
C	=	coefficient
C_A	=	axial force coefficient
C_{disp}	=	dispersed coefficient
CF	=	force coefficient
cg	=	center of gravity
C_l	=	rolling moment coefficient
CM	=	moment coefficient
C_m	=	pitching moment coefficient
C_{mq}	=	pitch damping coefficient
C_N	=	normal force coefficient
C_n	=	yawing moment coefficient
C_{nom}	=	nominal coefficient
C_{nr}	=	yaw damping coefficient
C_Y	=	side force coefficient
F	=	force
L_{ref}	=	reference length
M	=	moment
MRP	=	moment reference point
M_∞	=	freestream Mach number
OML	=	outer mold line
Re_d	=	Reynolds number w.r.t. diameter
SST	=	shear stress transport
T_∞	=	freestream temperature
t	=	time
t/T	=	normalized time
u_1, u_2	=	dispersion coefficients
u_{infl}	=	inflation rate coefficient
u_N	=	transient dispersion coefficient
V_∞	=	freestream velocity
v	=	velocity component
x, y, z	=	Cartesian components

Greek

α	=	angle of attack
α_T	=	total angle of attack
β	=	angle of sideslip
γ	=	ratio of specific heats
μ_∞	=	freestream dynamic viscosity
ρ_∞	=	freestream density
σ	=	standard deviation

Subscript

d	=	deployed
disp	=	dispersed
nom	=	nominal
s	=	stowed
trans	=	transient
x, y, z	=	Cartesian components

I. Introduction

EVERY successful mission to the surface of Mars has relied upon entry, descent, and landing (EDL) technologies derived from those developed in the 1960s and 70s for the Mars Viking program. While the successful 2012 landing of Mars Science Laboratory (MSL) demonstrated improvements in thermal protection systems (TPS), entry guidance, and propulsive terminal descent technologies, its aeroshell was near the size limit imposed by the launch vehicle payload shroud, and its supersonic parachute was the largest used to date. Increased payload masses and access to higher landing altitudes require alternate decelerator technologies. To this end, concepts including supersonic retropropulsion[1] (SRP), hypersonic inflatable aerodynamic decelerators[2] (HIAD), and supersonic inflatable aerodynamic decelerators[3] (SIAD) are being developed and matured to enable high-mass Mars EDL operations.

The Low Density Supersonic Decelerator (LDSD) program is designed to mature SIADs and new supersonic parachutes for use in low density atmospheres such as that of Mars. LDSD technologies are demonstrated with a supersonic flight dynamics test (SFDT) campaign during which two flight tests successfully delivered 6 m diameter robotic mission class SIADs (SIAD-R) to test conditions in June of 2014 and 2015. In both flights, a trailing ballute referred to as the parachute deployment device (PDD) was used to extract and deploy a large supersonic parachute. Although the parachute performance was off-nominal in both flights, the campaign was a success in demonstrating the flight system concept and evaluating SIAD-R performance.

Prior to flight, SFDT was simulated extensively with two flight simulation (FS) codes: Program to Optimize Simulated Trajectories II (POST2)[4] and Dynamics and Spacecraft Simulator for Entry, Descent and Surface Landing (DSENDS)[5]. The simulations were run in order to support vehicle development, conduct trade studies, and to target, evaluate, and optimize flight system performance. The focus of this paper is an overview of test vehicle (TV) aerodynamic models used in pre-flight simulations. Descriptions of the methodology used to generate each model and their implementation within the FS framework are presented. Comparisons are made between pre-flight predictions and aerodynamics reconstructed from flight data, and post-flight improvements to models are discussed.

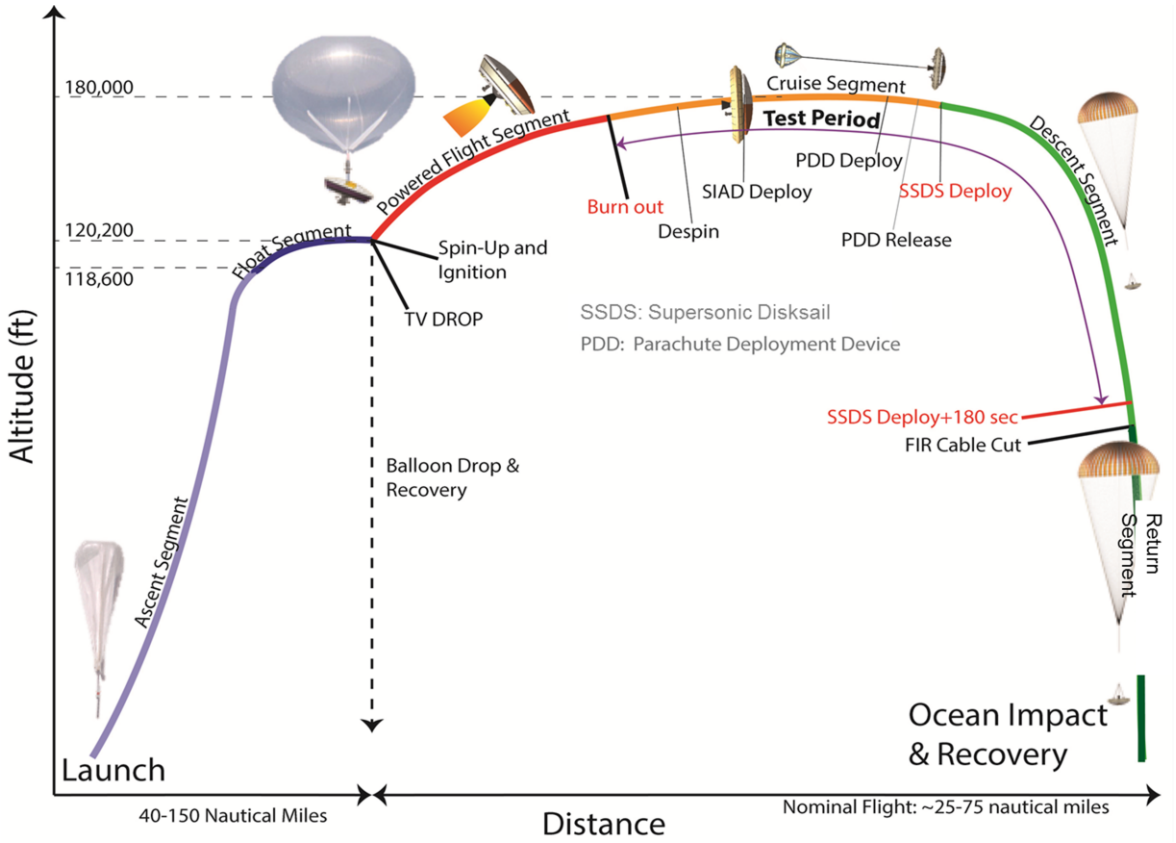

Figure 1. SFDT-1 concept of operations.

II. SFDT-1 Flight Operations and Test Vehicle

A. Flight Operations

LDSD flight operations, based at the Pacific Missile Range Facility (PMRF) on the Hawaiian island of Kauai, are similar to those of the Viking Balloon Launched Decelerator Test (BLDT) Program[6,7] conducted in 1972 Nominal SFDT flight, schematized in Fig. 1, begins with the inflation and deployment of a 34 million cubic foot helium balloon[8] which lifts the TV from a launch tower to a float altitude of approximately 36 km. The TV is suspended beneath the balloon at a hang angle which is targeted to produce a boost trajectory that will deliver the SIAD to its proper test conditions. Once desired balloon float conditions are met, the TV is released and spun up for gyroscopic stability. A boost motor is then ignited to accelerate the TV to Mach 4 and an altitude of approximately 53 km. After boost motor burnout, the TV is despun and the SIAD is deployed at a Mach number between 3.5 and 3.8. The TV then decelerates further before the PDD is deployed to extract the parachute at about Mach 2.5, whereupon the PDD is jettisoned and the remainder of the flight system decelerates to eventual splashdown.

SFDT-1 was flown on June 28, 2014. The flight trajectory lofted to an altitude of approximately 61 km, 8 km higher than predicted. SIAD-R deployed successfully at Mach 4.08 and flew for nearly 80 s, followed by successful PDD deployment and parachute extraction. The parachute, however, experienced structural failure during inflation.

SFDT-2 was flown on June 8, 2015, and lofted to about 2.9 km higher than predicted. It experienced an unidentified disturbance after despin that caused angle of attack oscillations of up to nearly 30°. Though the SIAD-R and PDD functioned nominally, the parachute failed a second time. Nevertheless, stable powered flight, SIAD deployment and stability, and PDD operation were successfully demonstrated, and a wealth of flight data were obtained from a variety of onboard and ground-based measurements.

B. Test Vehicle

The SFDT-1 TV, shown in Figs. 2 and 3, is a nonlifting blunt body configuration designed to deliver SIAD-R to supersonic test conditions which mimic those experienced during Mars entry. Detailed descriptions of the TV and its subsystems are documented in Ref. 8. With the SIAD stowed, the TV is a 4.7 m diameter axisymmetric aeroshell consisting of a spherical section forebody, conical aftbody, and an annular base plane surrounding a central aft-facing cavity. The 4.7 m diameter is a slight increase from the 4.5 m MSL aeroshell, and is the maximum size that can be accommodated for flight to Mars within an Atlas-V or Delta IV-H launch vehicle payload shroud[9]. The spherical forebody is similar to that of Orion, and possesses good drag performance and high volumetric efficiency.

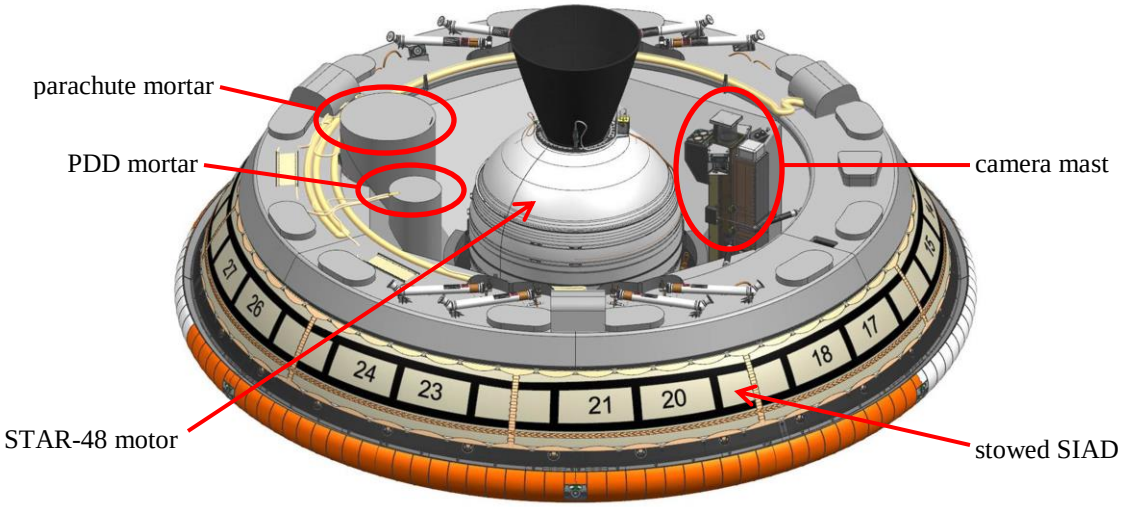

Figure 2. Isometric view, SFDT test vehicle aftbody with stowed SIAD-R. TPS blankets not shown.

At its periphery, the forebody is joined to a rounded shoulder fairing, which doubles as a radome and meets the aftbody across a small aft-facing step. The conical aftbody is "wrapped" with the stowed, uninflated SIAD, which is held in place with a retention and restraint cover prior to its deployment. Numerous hardware elements are mounted to the base plane, including spin and despin motors and their plume deflectors, PDD and parachute triple bridle assemblies, video cameras, and TPS blankets to protect sensitive components from spin, despin, and main motor

plume environments. An Alliant Techsystems Inc. (ATK) STAR-48B long nozzle SRM, its propellant mass reduced to yield the SFDT trajectory profile, is centrally mounted within the base cavity, flanked by a video camera mast and cylindrical mortars which house the PDD and parachute.

With SIAD-R deployed, the TV total diameter nominally increases to 6 m. SIAD-R is an attached torus constructed from 27 circumferential gores of silicone-coated Kevlar fabric and features a burble fence at its maximum diameter to ensure reliable flow separation and aerodynamic stability. SIAD deployment is accomplished with 9 pairs of gas generators, actuated sequentially in two pulses to first deploy and inflate the SIAD to shape, then to fully pressurize it. At its nominal fully inflated internal pressure of 28 kPa, the SIAD is essentially rigid at the upper bound 2.2 kPa dynamic pressure of flight, thus allowing for its modeling as a rigid body and making aerodynamic analysis straightforward with conventional numerical and ballistic range tools and methodology.

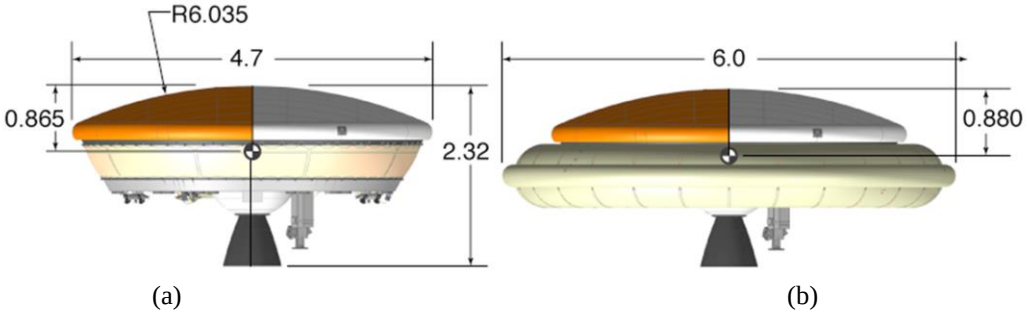

Figure 3. SFDT test vehicle with stowed (a) and deployed (b) SIAD-R. Dimensions in meters.

III. Aerodynamic Models

TV aerodynamic models are integrated within the FS framework with a routine referred to as the aerodatabase (ADB). The ADB contains aerodynamic models for all phases of the TV flight: drop, spin-up, powered ascent, coast, despin, SIAD inflation, and SIAD cruise. The models are implemented within the ADB with tables of aerodynamic coefficients, aerodynamic uncertainties, spin and despin motor plume interaction models, a SIAD inflation model, and supporting subroutines including table look-up, interpolation, and blend routines which act in concert to link the aerodynamics of all SFDT flight simulation phases together. At each time step in a flight simulation, the FS code passes arguments to the ADB including Mach number, dynamic pressure, center of gravity (*cg*) location, angles of attack α and sideslip β, uncertainty dispersions, and state flags for motor operation and SIAD

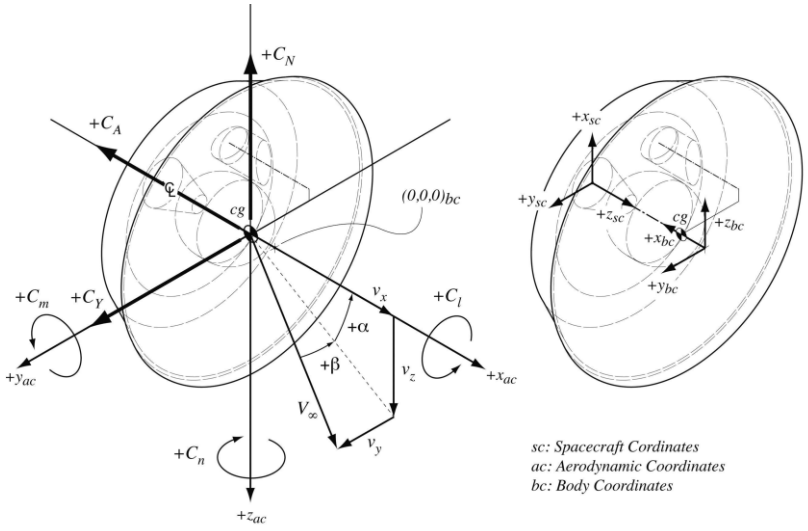

Figure 4. Coordinate system, aerodynamic angle, and aerodynamic coefficient conventions.

inflation. The ADB then interpolates aerodynamic coefficients from the appropriate tables, applies uncertainties and other models as required, and returns aerodynamic coefficients to the FS code.

TV aerodynamic models were constructed from computational and experimental data sources. Static aerodynamics were predicted with computational fluid dynamics (CFD) codes including the FUN3D[10], OVERFLOW[11], DPLR[12], and Loci-CHEM[13] flow solvers. Dynamic derivatives (i.e., pitch damping coefficients) for the TV in both stowed and deployed SIAD configurations were identified from ballistic range tests conducted in the Ames Research Center (ARC) Hypervelocity Free Flight Aerodynamics Facility (HFFAF)[14].

The ADB coordinate system, aerodynamic angle, and aerodynamic coefficient conventions are illustrated in Fig. 4. Moment coefficients tabulated within the ADB are expressed about the moment reference point (*MRP*), which is located on the axis of symmetry at the TV nose and is the origin of the body coordinate system (*BCS*). The *BCS* is referenced when passing *cg* location components to the ADB.

Aerodynamic uncertainty models within the ADB are formulated along the scheme used for MSL[15] as shown in Eq. 1. A dispersed coefficient C_{disp} is calculated from the nominal coefficient C_{nom} by applying an adder and multiplier, each perturbed independently with uncertainty dispersion coefficients u_1 and u_2 which range from -1 to 1 at the 3σ uncertainty limits.

$$C_{disp} = (C_{nom} + u_1 \cdot adder) \cdot (1 + u_2 \cdot multiplier) \qquad (1)$$

In a flight simulation, the dispersion coefficients are randomly generated with normal probability distributions and are held constant over the duration of the flight phase to which they apply. In FS Monte Carlo analysis, a new set of dispersion coefficients is generated for each run. Moment dispersions are applied at the *cg* so as to make them independent of moment transfer calculations.

Baseline uncertainties for the TV with deployed SIAD-R were chosen to be of the same magnitude as were used in the MSL ADB supersonic continuum regime uncertainty model[15]. Adder and multiplier 3σ uncertainty limits for all SFDT flight phases are tabulated in Table 1. Uncertainties for the powered phase are assigned in three distinct Mach regions, which allows for uncertainty sensitivity analyses partitioned by Mach number. Owing to the sensitivity of base drag to power-on effects, the powered phase C_A uncertainty model is split into forebody (f) and aftbody (a) contributions. The 3σ aftbody C_A uncertainty limits are equivalent to base pressure ranging from vacuum to freestream static, subject to an aftbody contribution upper limit C_A=5.

Flight phase		C_A	C_N, C_Y	C_m, C_n	C_{mq}, C_{nr}
Drop		±20%	±0.01, ±20%	±0.005, ±20%	n/a
powered	M_∞<0.25	f: ±2% a: 0-min(5, 2/γM^2)	±0.01, ±20%	±0.005, ±20%	n/a
	0.25≤M_∞≤1.5	f: ±2% a: 0-min(5, 2/γM^2)	±0.01, ±20%	±0.005, ±20%	n/a
	M_∞>1.5	f: ±2% a: 0-min(5, 2/γM^2)	±0.01, ±10%	±0.005, ±10%	n/a
Coast		±5%	±0.01, ±10%	±0.005, ±20%	±0.2
SIAD-R		±10%	±0.01, ±10%	±0.005, ±20%	±0.2

Table 1. Aerodynamic uncertainties for the SFDT test vehicle.

The following subsections describe the aerodynamic models for each TV flight phase, where references to event times correspond to those in nominal (undispersed) flight simulations.

A. Drop Phase

For aerodynamic modeling purposes, the nominal SFDT drop phase is defined as the interval which begins at the moment of release from balloon at *t*=0 s and ends at the moment of main motor ignition at *t*=2.15 s. During this period, the TV falls under the influence of gravity, and its total angle of attack is governed primarily by balloon hang angle and winds. The drop phase is of short duration and low freestream dynamic pressure, which pre-flight simulations predicted not to exceed 3 Pa. Hence, freestream aerodynamic forces and moments imparted to the test vehicle are very small, as are resultant pitch rates. Consequently, no pitch damping model is implemented for the drop phase. Spin is imparted to the TV by rocket motors during the drop phase, and aerodynamic increments due to spin motor plume impingement are added to drop phase aerodynamics by way of a separate model described below.

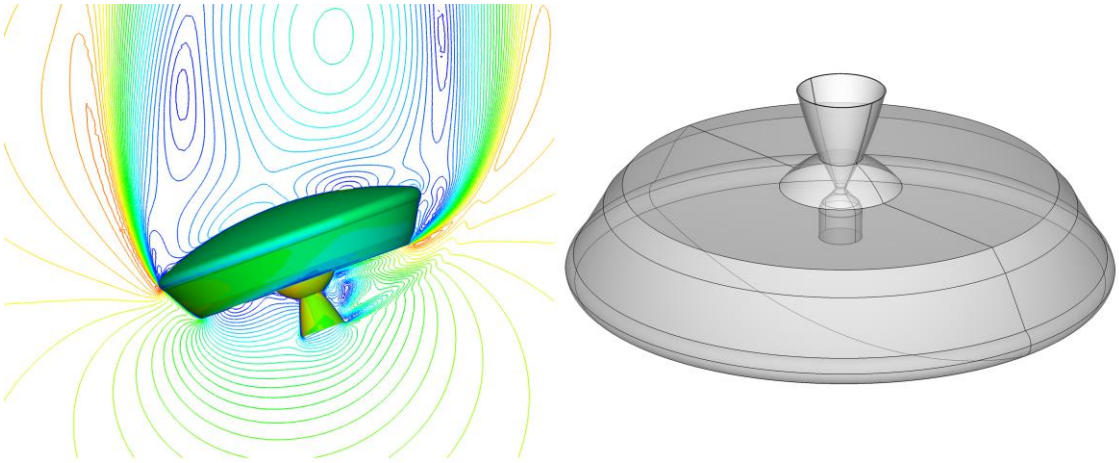

(a) (b)

Figure 5. a) Drop phase Mach contours. b) Geometry used in drop, powered, and coast phase analyses.

Drop phase static aerodynamics were modeled from CFD simulations run with the FUN3D code, using a laminar flow model, nominal 36 km atmospheric conditions, and a Mach number of 0.266 over an angle of attack range from 0° to 180° in 10° increments. Mach contours from a drop phase solution are shown in Fig. 5(a). The computational domain was discretized with a tetrahedral mesh of approximately 9 million nodes generated with the GridTool[16] and VGrid[17] codes, and TV surfaces were modeled as adiabatic viscous walls. As shown in Fig. 5(b), the outer mold line (OML) was a notional shape developed before the TV configuration was finalized, and lacked the aft-facing step, annular base cavity, and base plane protuberances of the flight article.

Aerodynamic uncertainties during the drop phase were chosen to be greater than the MSL baseline, as the freestream Mach number approaches zero, and computations at those conditions were not attempted for economical reasons. One-variable-at-a-time (OVAT) sensitivity studies conducted with POST2, however, indicated that SFDT flight performance would be tolerant of order-of-magnitude errors in drop phase aerodynamic predictions.

B. Spin-Up

SFDT-1 spin-up nominally begins with the ignition of a pair of spin motors at t=0.36 s. They have a burn time of about 0.25 s, and are followed by ignition of a second pair of motors at t=1.66 s, also with a burn time of 0.25 s. The cumulative angular momentum imparted to the TV results in a nominal spin rate of 300°/s, which gives the TV gyroscopic stability during the powered ascent phase.

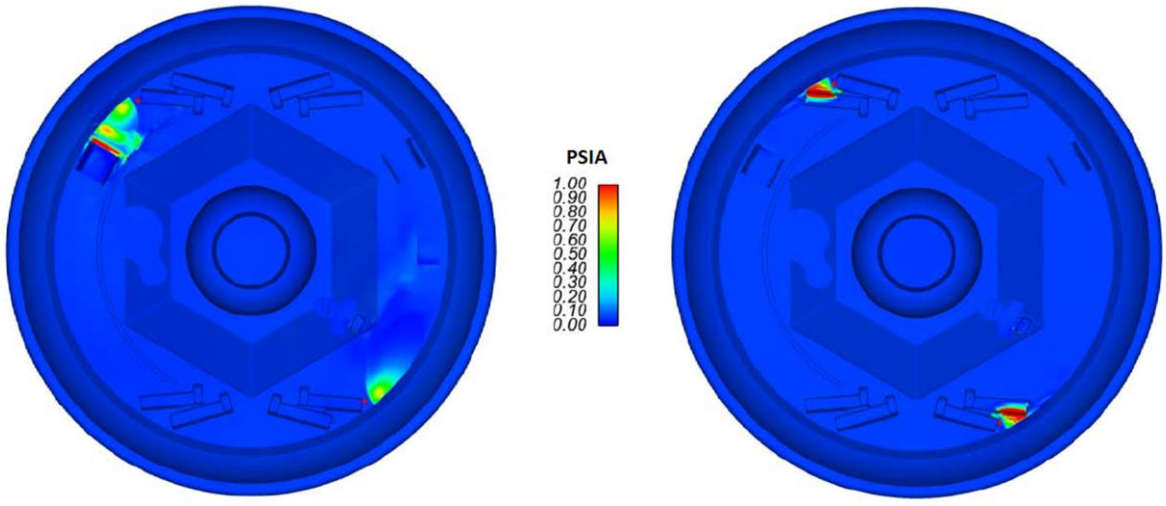

(a) (b)

Figure 6. Pre-flight model computed aftbody pressure contours for spin motors 1&3 (a) and 2&4 (b).

In many aerospace applications, plume flows generated by propulsive devices can impinge upon vehicle surfaces and/or interact with freestream flow, altering surface pressure distributions and producing unintended aerodynamic forces and moments[18,19]. The potential for such conditions arising as a consequence of spin motor operation was recognized as a possible source of rate and attitude error in early moments of SFDT flight which could result in an undesirable trajectory and failure to meet SIAD test conditions. CFD analyses were conducted to predict the extent of spin motor plume interaction and thus inform a model for use in flight simulations.

Pre-flight models of spin motor plume aerodynamic interactions were computed with a multi-code toolchain: the Reacting Multiphase Program (RAMP2)[20] and Boundary Layer Integral Matrix Procedure (BLIMPJ)[21] method-of-characteristics (MOC) codes, and the Loci-CHEM CFD code. The MOC codes were used to generate nozzle flow solutions, which in turn were used to prescribe nozzle boundary conditions for the Loci-CHEM simulations. Unstructured grids for Loci-CHEM were generated from CAD models using ANSA, SolidMesh, and AFLR3[22], and were highly detailed, with the final volume grids containing over 170 million cells. Viscous wall boundary conditions were used, with adiabatic nozzle surfaces and constant temperature (255 K) walls elsewhere. A frozen chemistry gas model was used with freestream air and surrogate exhaust gas species. The freestream was initialized with nominal 36 km atmospheric conditions at a Mach number of 0.05 and 0° angle of attack. A Reynolds-Averaged Navier-Stokes (RANS) scheme with SST turbulence model was used to compute the solutions, advanced second order in time until convergence to a steady flow state was attained. Plume-induced forces and moments were calculated by taking the difference between cases converged with and without the plume flows, neglecting spin motor thrust surfaces in all cases. Computed pressure contours on the backshell for each spin motor pair are shown in Fig. 4. Dimensional spin motor interaction forces and moments are tabulated in Table 2, where moments are expressed about the *MRP*.

motors	F_x	F_y	F_z	M_x	M_y	M_z
1 + 3	39.3	-260.4	308.9	-1098.9	160.4	692.5
2 + 4	508.5	25.2	-61.4	-1350.9	-80.8	-11.4

Table 2. Spin motor model plume induced forces (N) and moments (N*m) in aerodynamic coordinate system.

In the flight dynamic simulations, spin motor plume interaction models are activated by passing flags to the ADB during each motor pair burn. The interactions are calculated within the ADB from the entries in Table 2, which are converted to coefficient form using the instantaneous reference conditions. Resultant moment coefficients about the *cg* are then calculated, dispersed normally with a ±20% uncertainty at the 3σ uncertainty level, transferred back to the *MRP*, and added to the drop phase moment coefficients. Besides their use in calculating moment coefficient increments about the *cg*, force coefficient increments are neglected, as their effect on the TV trajectory is negligible.

C. Powered Phase

The powered flight phase begins at the moment of STAR-48 ignition and ends at burnout, which for FS modeling purposes is defined as the moment when TV axial acceleration crosses zero. The production STAR-48B[23] is a SRM with an average thrust of 68.6 kN over a burn of 84.1 s, however the SFDT-1 flight motor propellant grain was offloaded by about 400 kg to reduce burn time to approximately 68 s and yield the desired trajectory. During a nominal powered phase, the TV gains approximately 17 km of altitude, its Mach number increases from about 0.04 to 4, and its total angle of attack decreases from 150° to about 2°. Over 1600 kg of propellant is burned from the offloaded motor, reducing the TV total mass by about half. The STAR-48 plume becomes increasingly underexpanded with increasing altitude, and nearly fills the wake region just prior to burnout.

The pre-flight powered phase aerodynamic model was constructed at trajectory points taken from an early flight simulation and tabulated in Table 3. A combination of Orion[24] aerodynamics and FUN3D solutions were used to populate the sub- and transonic solution space, and the OVERFLOW code was used to compute trans- and supersonic regime solutions. At the overlap Mach number of 0.91, aerodynamics were averaged between results from the two codes. In addition to the powered solutions, power-off solutions were computed at all points for use in other flight phase models. For lack of supporting data, no powered phase pitch damping model was implemented.

M_∞	V_∞ (m/s)	ρ_∞ (kg/m^3)	T_∞ (K)	μ_∞ (N·s/m^2)	Re_d	α_T
0.266	82.6	6.664E-03	239.4	1.544E-05	1.676E+05	0°-180°
0.505	156.9	6.293E-03	240.4	1.549E-05	2.996E+05	0°-60°
0.905	283.2	5.190E-03	245.5	1.576E-05	4.384E+05	0°-40°
1.507	478.0	3.480E-03	253.0	1.614E-05	4.844E+05	0°-30°
2.486	800.7	2.199E-03	262.0	1.660E-05	4.985E+05	0°-20°
4.037	1309.3	1.466E-03	269.8	1.700E-05	5.306E+05	0°-20°

Table 3. Flow conditions for powered phase aerodynamic model.

All pre-flight powered phase aerodynamic computations analyzed the same simplified axisymmetric OML as was used for drop phase computations, which omitted the base cavity and other geometric features of the flight article. TV spin was not modeled in the simulations. Surface grids were configured with separate domains for fore- and aftbody regions so that their aerodynamic contributions and uncertainties could be independently accounted for and dispersed. Convergent-divergent nozzle flows were computed for all powered cases, using subsonic total pressure, total temperature inflow boundary conditions applied to a plane upstream of a convergent plenum. At the time of analysis, flight motor properties were not fully known, so nominal thrust and chamber pressure were assumed to take average values during the burn, held constant at all trajectory points. In calculating the powered phase aerodynamics, thrust surfaces were omitted from the force and moment summation so as to isolate the aerodynamics from thrust. The STAR-48 thrust model used in flight simulations resides in the FS codes and is not used in any way by the ADB. Mach contours from FUN3D and OVERFLOW solutions are shown in Figure 7.

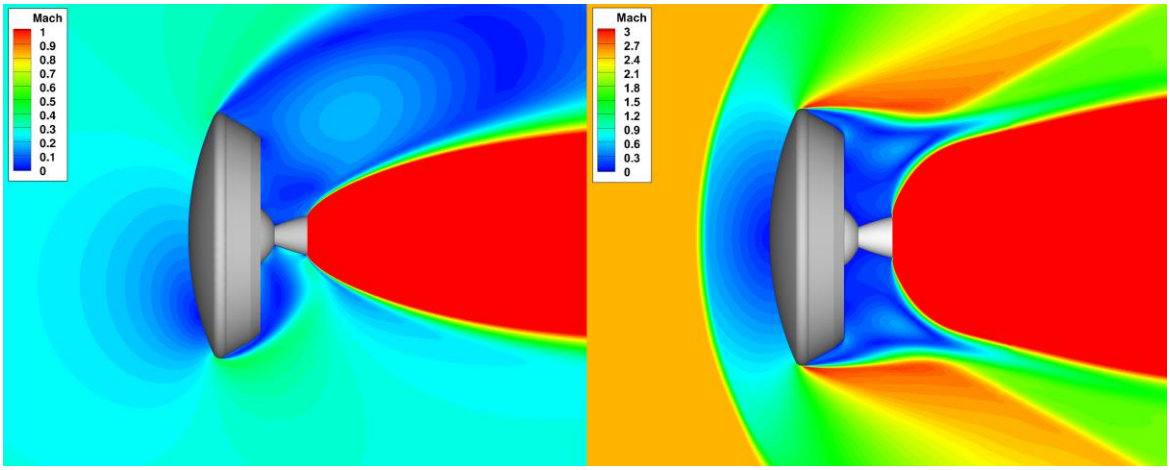

(a) (b)

Figure 7. Powered phase solution Mach contours: a) Mach 0.266, α=30°; and b) Mach 2.486, α=0°

FUN3D sub- and transonic powered phase solutions were computed on fully tetrahedral grids of about 9 million nodes using a Roe flux scheme, Menter-SST turbulence model, Van Leer flux limiter, and no-slip adiabatic walls. A calorically perfect, single species gas model with γ=1.4 was used for both freestream and exhaust gas. Nozzle inflow total temperature was set to 3520 K and the total pressure was adjusted to yield 66 kN thrust. In order to avoid solution divergence at the plenum inflow boundary, the computational procedure required several restarts, each with an increase in total inflow conditions until the desired thrust was obtained. The solution was then advanced with a global time step until a steady aerodynamic solution was obtained, or in the case of an unsteady solution, advanced over a sufficient number of iterations to capture the mean aerodynamics. At the Mach 0.266 condition, the nozzle flow entrained the freestream such that velocity and angle of attack were influenced upstream to a distance which increased with simulation time. This feature reduced confidence in the solutions, so aerodynamics for this Mach

number were taken from Orion data and adjusted with an axial force coefficient increment ΔC_A=0.91 taken from a power-on computation at zero angle of attack.

OVERFLOW trans- and supersonic regime solutions were computed on an overset grid system of about 34 million points using a central differencing scheme, Baldwin-Barth turbulence model, no-slip adiabatic walls, and a two-species gas model with freestream γ=1.4. A nominal chamber pressure of 568 psia and exit exhaust gas γ=1.21 were assumed, the latter based on properties of an aluminized ammonium perchlorate-HTPB propellant. The nozzle inflow boundary condition was thus specified with a resultant net thrust of 58 kN. Though lower than nominal thrust for the standard Star-48 motor, this value was used as it became known that 1) the flight motor would not be a standard, off-the-shelf item due to propellant offloading; and 2) computed power-on effects were relatively insensitive to small differences in thrust. The computational procedure required several restarts, incrementally increasing nozzle inflow pressure and temperature in order to avoid solution divergence. Computations were advanced with a local timestepping scheme until aerodynamics were converged to a steady state.

Plume-induced effects observed in the powered phase solutions included increases in axial force and pitch stiffness. As the STAR-48 plume entrains the TV wake flow, it reduces the base pressure by aspiration[25] and thus increases drag. As shown in Fig. 8, the base flow scavenging effect becomes biased to the windside (lower half of the figure) at angle of attack, further reducing pressure there and strengthening the pitching moment in comparison to the case with no plume. Consequently, the TV in simulation has a tendency to turn into the wind more readily when the motor is firing. Plume flow effects are strongest in the sub- to transonic regime, and become insignificant with increasing Mach number as the TV total angle of attack decreases and aerodynamics become dominated by the forebody flow.

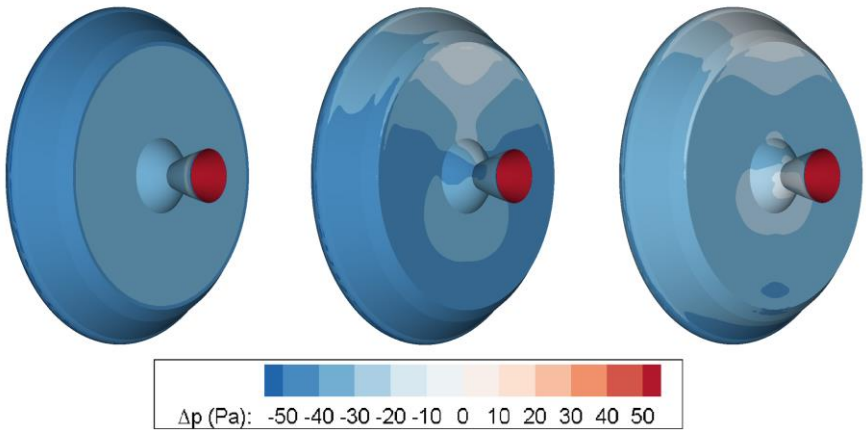

Figure 8. Power-on base pressure effects: Mach 0.505 at 0°, 10°, and 20° angle of attack.

In flight simulations, the transition from powered phase to coast phase aerodynamics and uncertainties at the end of the STAR-48 burn is implemented over the approximate thrust tail-off interval of 0.25 s which begins at the moment of burnout. During this interval, the FS code passes a dimensionless transition time $0 \le t \le 1$ to the ADB which is then used to blend aerodynamic coefficients and uncertainties along S-curves calculated by Eq. 2.

$$C = C_{powered} + (C_{coast} - C_{powered})(1 - (1 + \cos(\pi t))/2) \qquad (2)$$

D. Coast

The coast phase is defined as the time between STAR-48 burnout and the onset of SIAD inflation. Coast nominally begins at about Mach 4 and lasts for approximately 6 s. Despin occurs during the coast phase and is treated with a despin motor plume interaction model described below. Coast phase static aerodynamics were taken from power-off OVERFLOW and FUN3D solutions. Additional supersonic high-alpha solutions were computed for the derivation of tumbling TV drag in off-nominal scenarios. The coast phase pitch damping model was derived from ballistic range data[14] compiled over 12 shots at Mach numbers from 3.16 to 3.67.

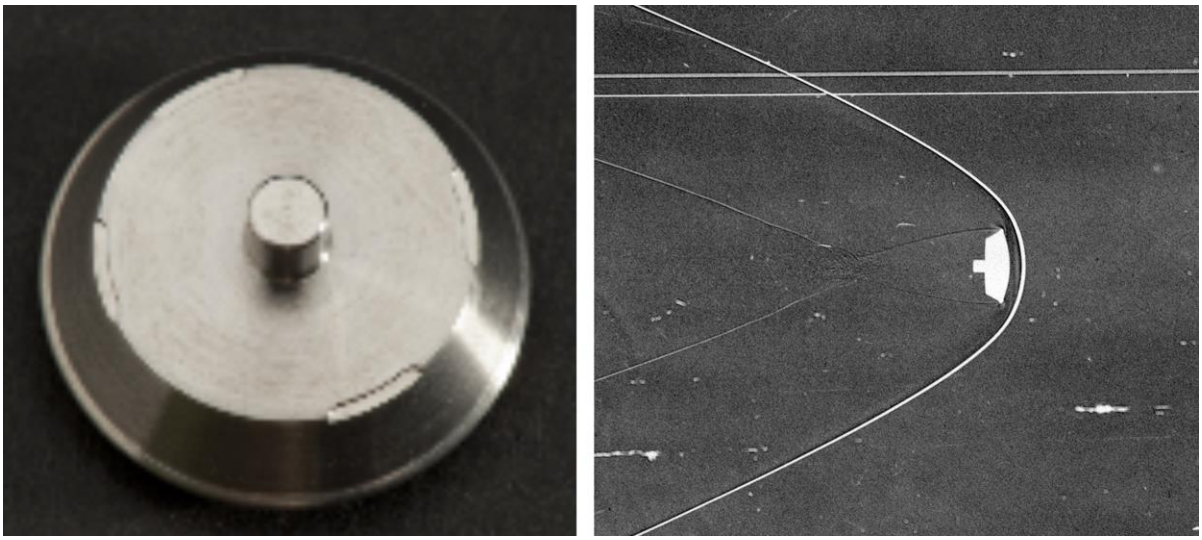

(a) (b)

Figure 9. a) Coast phase ballistic range model, and b) shadowgraph from Mach 3.15 shot.

E. Despin

Despin occurs during the coast phase and nominally reduces the TV roll rate to zero by action of two pairs of despin motors. Despin motor plume interactions were computed with the Loci-CHEM CFD code in much the same manner as the spin motor interactions, but with the despin motor geometry and at different freestream conditions. Despin flowfield solutions were generated for the TV with a 342°/s roll rate, at zero angle of attack and Mach 4.24 in a 50 km atmosphere. Despin model implementation is identical to that of the spin-up model, though with a larger 3σ uncertainty of ±40% distributed normally. The larger uncertainty is intended to reflect the greater dynamic pressure and thus potential for interaction with the freestream at despin conditions, in addition to angle of attack variability in the flight simulations. Predicted despin motor plume-induced forces and moments are tabulated in Table 4, where moments are expressed about the *MRP*. In flight simulations, TV dynamics had low sensitivity to the despin plume model interactions.

motors	F_x	F_y	F_z	M_x	M_y	M_z
5 + 7	3731.5	16.0	-1.1	603.9	-4.5	-8.1
6 + 8	3461.8	169.4	224.2	762.9	252.6	-341.1

Table 4. Despin motor model plume induced forces (N) and moments (N*m) in aerodynamic coordinate system.

F. SIAD Inflation

For modeling purposes, the SIAD inflation phase is defined as the event that begins at the onset of SIAD deployment and ends when the SIAD has reached its design shape and internal pressure. At nominal test conditions, full SIAD-R inflation occurs in about 0.4 s.

The pre-flight SIAD-R inflation model is based upon results published by Bohon and Miserentino[26], who conducted wind tunnel experiments with attached inflatable decelerators. The inflation model consists of two primary components: a transition from stowed to deployed SIAD aerodynamics, and a transient disturbance arising from asymmetric SIAD deployment.

The aerodynamic transition between stowed and fully deployed SIAD states follows an S-curve which in principle follows the change in overall vehicle shape and size. This transition is modeled over the inflation time T during which the position within the interval t/T is passed from the FS code to the ADB. In the flight dynamic simulations, A_{ref} and L_{ref} are changed to deployed SIAD values at the beginning of SIAD inflation, and aerodynamic force and moment coefficients are blended using Eqs. (3) and (4), where subscripts s and d correspond to stowed and deployed SIAD, respectively. The inflation rate coefficient u_{infl} is dispersed normally over ±1 and changes the shape of the inflation blend curve. The dimensionless blend fraction is plotted with its ±3σ dispersions in Fig. 11.

$$CF = \frac{(CF \cdot A_{ref})_s}{(A_{ref})_d} + \left[CF_d - \frac{(CF \cdot A_{ref})_s}{(A_{ref})_d} \right] \left(1 - \left(\frac{1+\cos[2\pi(t/T)]}{2} \right)^{1+0.3u_{infl}} \right) \tag{3}$$

$$CM = \frac{(CM \cdot A_{ref} \cdot L_{ref})_s}{(A_{ref} \cdot L_{ref})_d} + \left[Cm_d - \frac{(CM \cdot A_{ref} \cdot L_{ref})_s}{(A_{ref} \cdot L_{ref})_d} \right] \left(1 - \left(\frac{1+\cos[2\pi(t/T)]}{2} \right)^{1+0.3u_{infl}} \right) \tag{4}$$

The transient disturbance model is also based upon data from Ref. 26, in which a substantial transient normal force coefficient (C_N=0.2) was recorded during inflation with the SIAD at zero angle of attack. The model assumes a normal force disturbance applied in a random radial direction and a correlated moment equivalent to "blanking" a 40° sector of the SIAD, intended to simulate failure of a pair of gas generators. The disturbance takes the shape of a wave, and its magnitude is dispersible from 0-100% via coefficient u_N with a uniform probability distribution. Transient normal force and moment coefficients are modeled with Eqs. (5) and (6), and the undispersed time-varying normal force coefficient is plotted in Fig. 11.

$$C_{N,trans} = 0.2 \cdot u_N \left(\frac{1-\cos[2\pi(t/T)^{0.3}]}{2} \right)^8 \tag{5}$$

$$C_{m,trans} = 0.191 \cdot C_{N,trans} \tag{6}$$

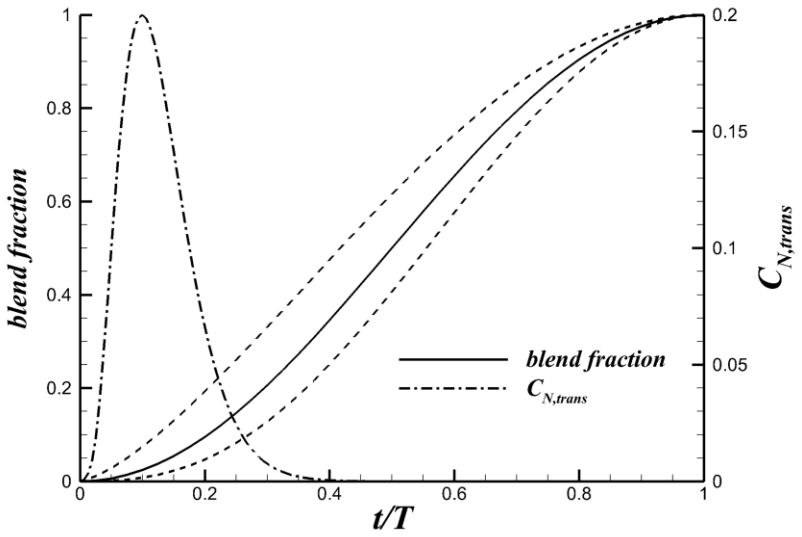

Figure 11. SIAD inflation and transient disturbance model curves.

G. SIAD-R Cruise Phase

The SIAD-R cruise phase begins at full inflation and continues until parachute deployment. At the nominal ratio of internal pressure to freestream dynamic pressure, the fully inflated SIAD-R behaves much like a rigid body, as demonstrated in rocket sled testing[27] where peak measured deformations were on the order of 30 mm. This aspect of SIAD-R makes it relatively simple to analyze in comparison to larger, ram-air inflated isotensoids which require deformed OML analysis[28].

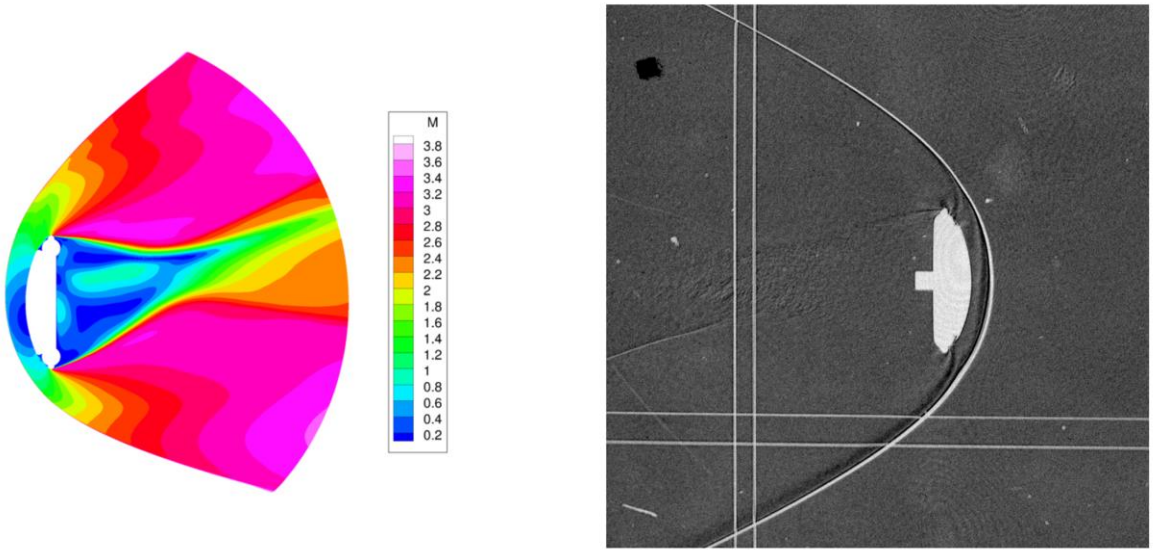

(a) (b)

Figure 12. SIAD cruise: a) computed flight Mach contours and (b) ballistic range shadowgraph.

As detailed in Ref. 29, SIAD-R cruise static aerodynamics were modeled from CFD simulations run with the DPLR code, using the Menter-SST turbulence model for nominal flight conditions at Mach 3.97, 3.0, and 2.12. Solutions were computed at angles of attack from 0° to 30° with 10° increment for the Mach 3.97 condition, and from 0° to 90° in 15° increment for the other Mach numbers. Four OMLs were analyzed, including two idealized axisymmetric geometries: one with a flat base and one with the STAR-48 nozzle; and two as-measured geometries taken from laser scans of the inflated SIAD-R, gridded to resolve individual SIAD gores and determine the effect of the geometry on aerodynamics and aeroheating. All geometries omitted the base cavity and protuberances. Hyperbolic grids of the idealized flat base and nozzle-included geometries contained about 10 million and 13 million points, respectively, while the laser scan grids contained about 59 million points to capture geometric detail. Aerodynamic variance due to differences between OMLs was within 3%. Solutions exhibited unsteady flow features due to separation and reattachment at the aeroshell-SIAD interface and burble region, and massive wake flow separation. Aerodynamic variances due to flow unsteadiness were about 1% of the means.

The SIAD-R cruise phase pitch damping model was derived from ballistic range test results[14] compiled from 37 shots at Mach numbers from 2.03 to 3.85.

IV. Comparison of Models to Reconstructed SFDT-1 Flight Data

SFDT-1 flight data were collected from a variety of sources, including meteorological balloons and sounding rockets, on-board inertial measurement unit (IMU) and global positioning system (GPS), and ground-based tracking radars. With atmospheric properties reconstructed from meteorological measurements, the remainder of the data were combined with thrust and mass models to reconstruct the trajectory and aerodynamics using NewSTEP[30]. NewSTEP is an Iterative Extended Kalman Filter (IEKF) code that has seen use in reconstruction activities for many noteworthy flight projects, including Hyper-X, Ares I-X, and MSL[31-33].

The powered phase presented a particular challenge to the aerodynamic reconstruction effort. The STAR-48 motors were offloaded specifically for SFDT, hence the predicted thrust curve models were not backed up with flight data. A chamber pressure transducer intended for use in the STAR-48 thrust reconstruction was not flown due to an electrical malfunction. With the flight thrust profile unknown, errors in the SFDT-1 pre-flight thrust and aerodynamic axial force models could not be separated. In the final reconstruction, adjustments were made to the thrust model such that combined thrust and axial force would yield the reconstructed axial accelerations.

Aerodynamic predictions are compared against reconstructed aerodynamics in the following sections, where the pre-flight production ADB (version 1.3.4) is called at reconstructed flight conditions at each time step. Reconstructed data are from NewSTEP SFDT-1 run 5.5 and are interpolated to 100 Hz. For brevity, ADB refers to pre-flight aerodynamic models, and BET (best estimated trajectory) refers to reconstructed quantities. All moments and moment coefficients are about the reconstructed *cg*. It should be noted that the reconstructed aerodynamics are based on measured accelerations and rates, where contributions from spin, despin, and boost motors are not separated from those due to aerodynamics.

A. Drop and Spin-Up Phase

The drop and spin-up phase BET axial force and total angle of attack plotted in Fig. 13(a) show results which illustrate a limitation of the reconstruction method in the very low speed regime. Under- and overshoots seen at the edges of balloon drop and spin motor events are filtering artifacts. The spin motor events are readily identifiable in the axial force trace due to the aft nozzle cant, a feature intended to protect the TV from plume impingement. The component of axial force due to external aerodynamics is small and does not appear to be of the expected sign, and the problem of reconstructing aerodynamics at near-zero dynamic pressures is recognized.

Assuming equal spin motor thrusts and symmetric thrust vector alignments, the spin-up model is assessed by subtracting ADB drop phase pitch and yaw moments from the respective BET moments, then comparing the remainder to spin model moments resolved about the *cg*. The comparison is made for the first spin motor pair, which is predicted to produce the larger pitch and yaw interactions. As plotted in in Fig. 13(b), the comparison does not provide conclusive evidence as to whether or not the model correctly predicts the sign or magnitude of spin motor plume interactions. The reconstructed interactions cannot be definitively quantified due to numerical oscillations.

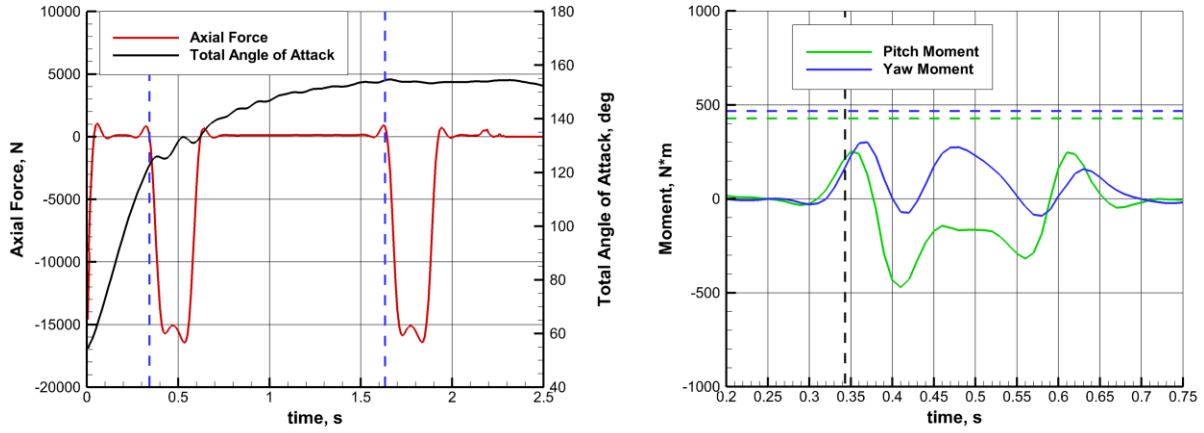

(a) (b)

Figure 13. a) Reconstructed drop phase axial force and total angle of attack, and b) spin-up interaction pitch and yaw moments, where vertical dashed lines denote ignition commands, and horizontal dashed lines denote model pitch and yaw moment values.

B. Powered Phase

During the powered phase, the reconstructed side and normal force data are extremely noisy and difficult to interpret during the first few seconds, so we restrict our analysis to the period $t \geq 10$ s. BET side and normal force coefficients are plotted in Fig. 14(a). Biases are apparent in both reconstructed coefficients, which should oscillate about zero while the TV is spinning due to axisymmetric aerodynamics. The biases persist over the duration of the burn, and are roughly proportionate to the thrust coefficient, suggesting a thrust misalignment of approximately 0.1° with respect to the spin axis, well within the uncertainty limit of 0.3°. In Fig. 14(b), the BET moment coefficients are plotted and biases are seen in these coefficients as well. Omitted for clarity, the ADB moment and normal force coefficients oscillate about zero throughout the powered phase.

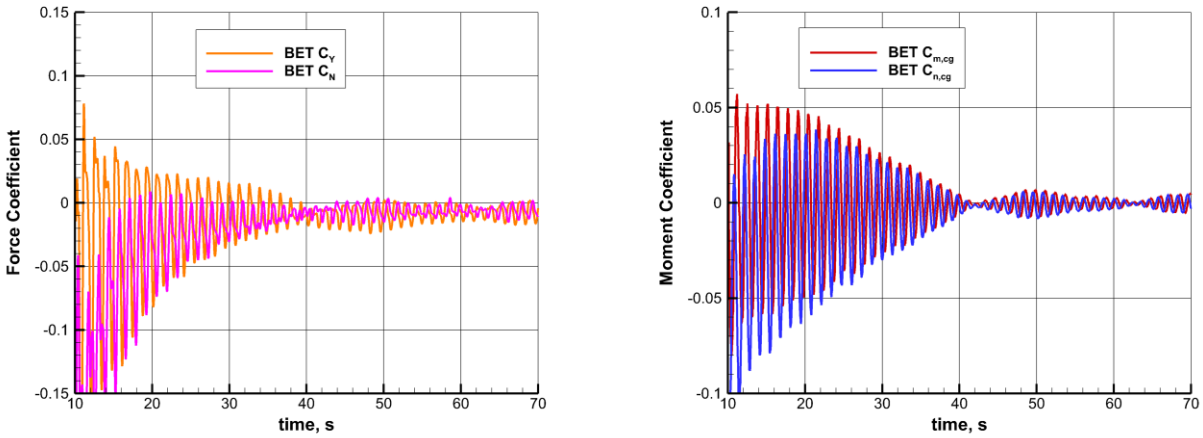

(a) (b)

Figure 14. Reconstructed a) side and normal force coefficients, and b) pitch and yaw moment coefficients.

Reconstructed angles of attack and sideslip plotted in Fig. 15(a) are symmetric. Combined with a lack of persistent bias in moment coefficients, this feature may indicate a thrust misalignment which counters the effect of a radial *cg* offset. The mean total normal force is nearly constant and its correlation to total angle of attack is weak, as shown in Fig. 15(b). Because the normal force signal contains a great deal of noise and is modified by data smoothing, a definitive cause for the bias is unidentifiable, however it is likely a combination of radial *cg* offset and thrust misalignment.

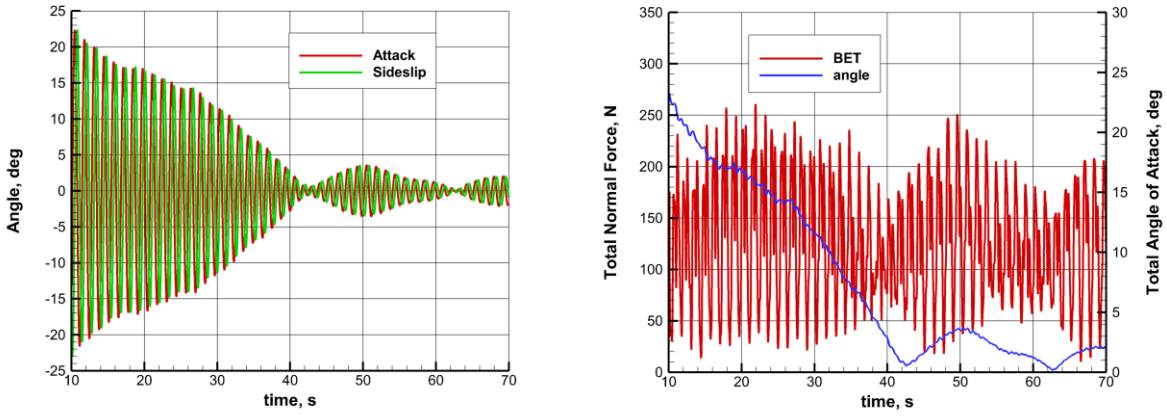

(a) (b)

Figure 15. a) BET angles of attack and sideslip, and b) total normal force and angle of attack.

A comparison of BET and ADB total moment coefficient plotted in Fig. 16 shows two important features: oscillations in the flight data indicate wobbling, and the moment coefficient was overpredicted. The latter is of particular importance, as a strong pitching moment would cause the TV to point more readily into the freestream velocity vector at angle of attack, resulting in a lower flight path angle. Hence, flight simulations predicted a lower peak altitude than was flown. Post-flight analyses indicated that the overpredicted moment coefficient was a significant contributor to SFDT-1 lofting[34].

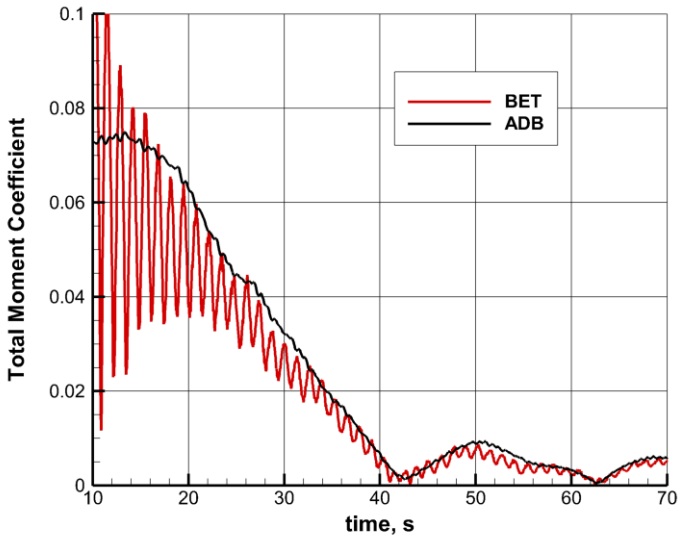

Figure 16. Total moment coefficients.

C. Coast

According to reconstruction, the SFDT-1 coast phase took place over the interval $73.0 \leq t \leq 82.5$ s, during which time the Mach number decreased from 4.29 to 4.09, the dynamic pressure decreased from 556 Pa to 333 Pa, and the TV total angle of attack ranged from 0.18° to 3.05°. Over this range of conditions, the ADB queries a single table corresponding to OVERFLOW solutions run at Mach 4.04. As shown in Fig. 17(a), the reconstructed axial force coefficient changes by 4.2% over the interval and at maximum exceeds predictions by about 3.3%. Variability in the axial force may be due to STAR-48 thrust tail-off, atmospheric variability, or a combination of the two. The reconstructed normal force is in good agreement with predictions as shown in Fig. 17(b).

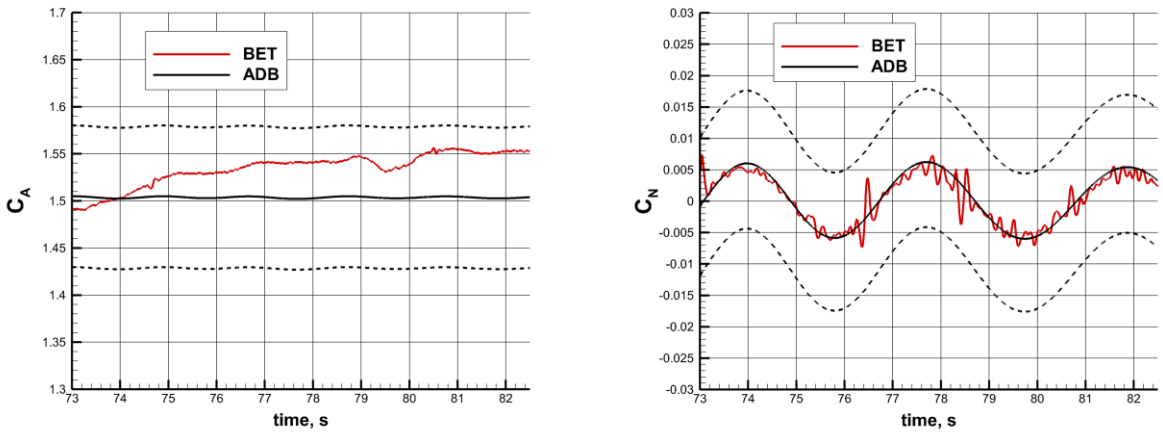

(a) (b)

Figure 17. a) Axial force and b) normal force coefficients, dashed lines denote model 3σ uncertainties.

The pitching moment coefficient is also in excellent agreement with predictions as shown in Fig. 18(a). A bias in the reconstructed yawing moment is correlated to a nonzero sideslip trim angle shown in Fig. 18(b). The trim angle of sideslip is approximately -0.5° and could be due to a radial *cg* offset about -0.0035 m along the y-axis.

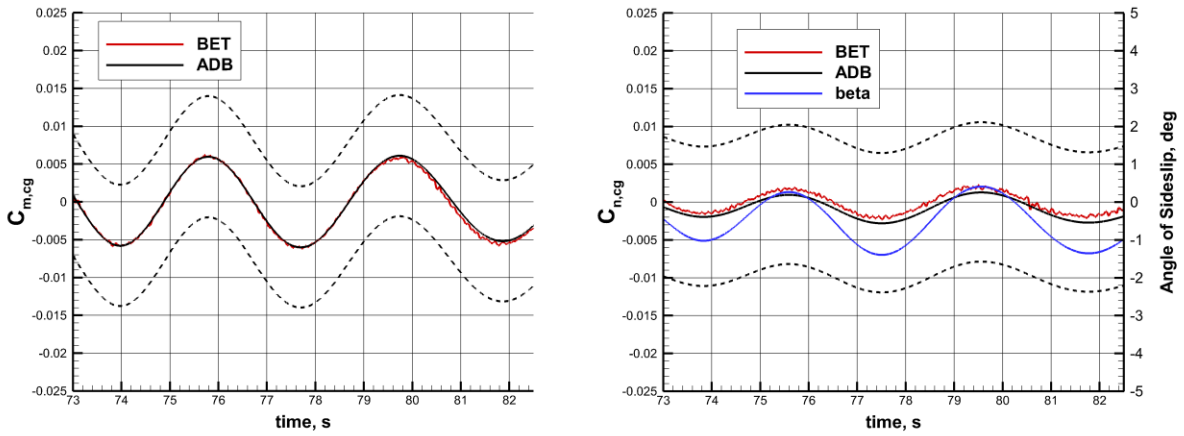

(a) (b)

Figure 18. a) Pitching moment coefficients and b) yawing moment coefficients with nonzero sideslip trim angle. Dashed lines denote model 3σ uncertainties.

D. Despin

Flight reconstruction indicates that despin motor firings occured at approximately t=72.05 s and t=72.55 s, where motors 6 & 8 are fired before motors 5 & 7. Similar to the spin motor result, the reconstructed despin motor axial force disturbance shows evidence of filtering artifacts as shown in Fig. 19(a). The despin model predicted a substantial yaw moment interaction for the first motor pair and negligible interactions for the second pair. The predicted yaw moment is denoted by the dashed line in Fig. 19(b). In this case, it appears that numerical under- and overshoots are swamping the desired signal. Analysis of isolated accelerations and mechanical vibrational modes is probably required to accurately quantify despin motor interaction and is beyond the scope of the current work.

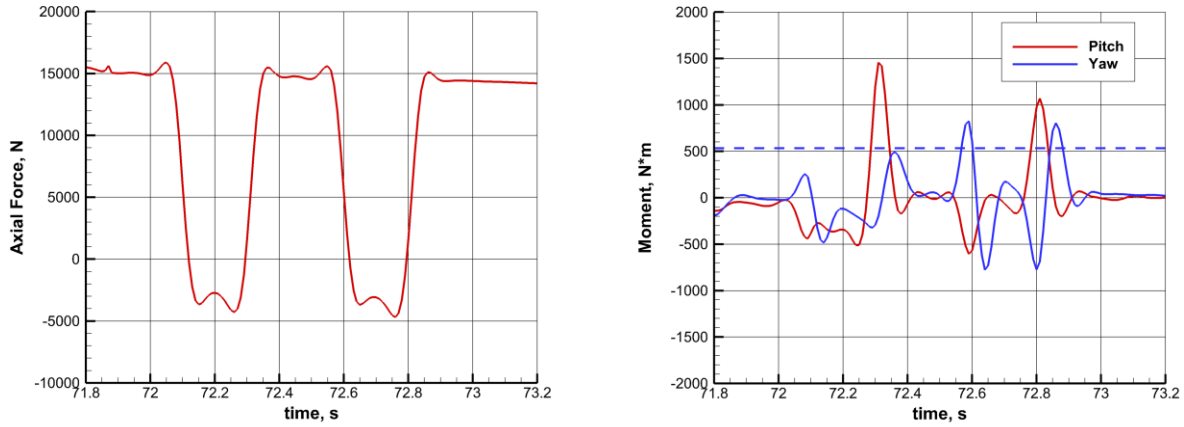

(a) (b)

Figure 19. Reconstructed despin a) axial force disturbance, and b) interaction pitch and yaw moments, where the dashed line denotes the predicted yaw moment.

E. SIAD Inflation

The reconstructed axial force trace plotted in Fig. 20(a) indicates that the SIAD-R inflation began at approximately t=82.6 s. The reconstruction here suffers from the same under- and overshoots seen in other transient events, e.g., drop, spin, and despin. There is no aerodynamic explanation for these oscillations, however mechanical modes and structural ringing are likely contributors to these behaviors. We conclude that the method of reconstruction is not amenable to transient events, and so rather look to the aerodynamic angle history to assess the inflation model. The reconstructed angles of attack and sideslip are plotted In Fig. 20(b). An increase of pitch rate is seen as expected, however the pitch angle amplitude growth that would be expected to accompany an asymmetric SIAD deployment is not observed.

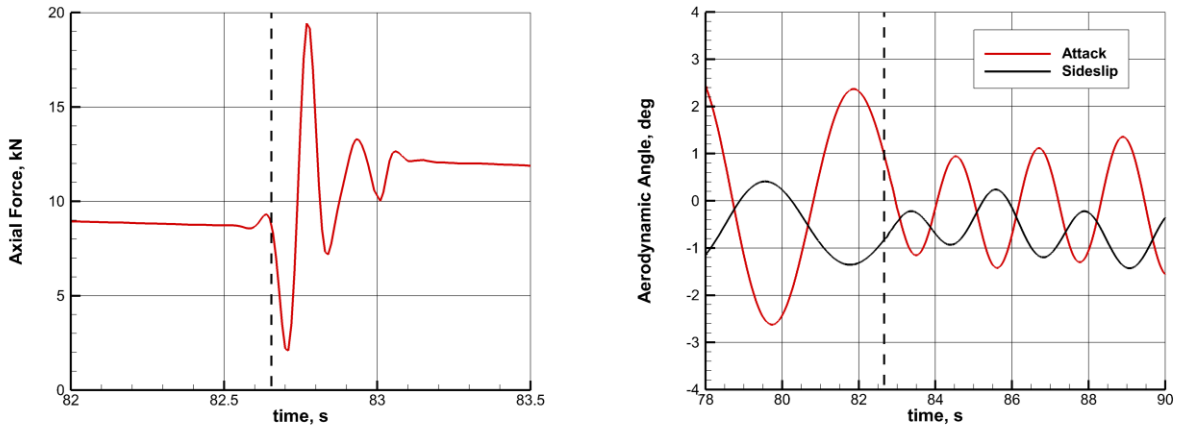

(a) (b)

Figure 20. Reconstructed a) axial force during SIAD inflation, and b) aerodynamic angle history showing increase in pitch frequency after SIAD inflation, where vertical dashed line denotes start of inflation.

As shown in Fig. 21, activating the inflation transient model to its 3σ limit in simulation perturbs the vehicle and suddenly increases the pitch angle amplitude. This perturbation was not observed in flight, and it is concluded that SIAD deployment was nominal.

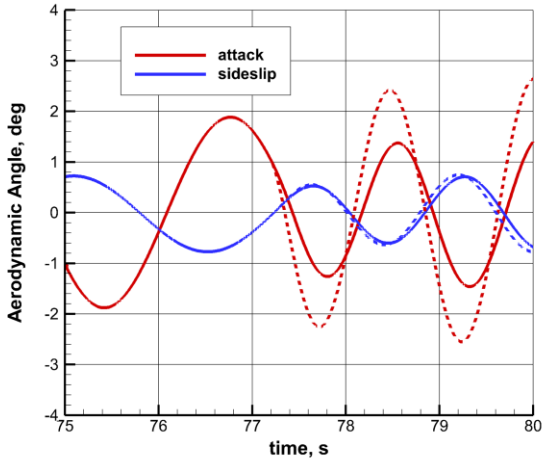

Figure 21. Inflation event in simulation, with nominal inflation denoted by solid lines, and transient model at 3σ limit denoted by dashed lines.

F. SIAD Cruise

The SIAD cruise phase began after full inflation at about t=83.1 s and ended at approximately t=161.3 s, just before PDD deployment. During this time, the Mach number decreased from 4.06 to 2.73, the dynamic pressure decreased from 317 to 151 Pa, then rose again to 422 Pa as the TV gained, then lost, altitude. The TV total angle of attack ranged from less than 0.1° to 2.75° during cruise. As shown in Fig. 22(a), the reconstructed coefficient falls well within 3σ model uncertainties and is correlated with freestream dynamic pressure as shown in Fig. 22(b).

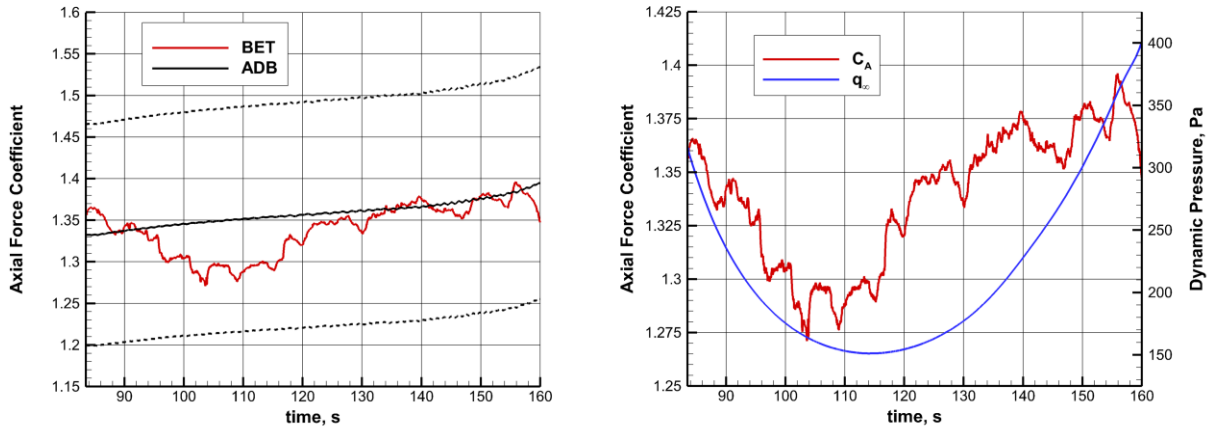

(a) (b)

Figure 22. SIAD cruise phase a) axial force coefficient, with 3σ model uncertainties denoted by dashed lines, and b) reconstructed axial force coefficient and freestream dynamic pressure.

Reconstructed pitching and yawing moment coefficients are compared against the model values in Fig. 23. The reconstructed amplitudes exceed those of the model, implying that the model moment curve slopes are shallow. Additionally, the moment coefficients oscillate symmetrically about zero, while the reconstructed angle of sideslip is nonzero. As shown over a 30 s interval in Fig. 24, the sideslip trim angle is approximately -0.5° and could be caused by a radial *cg* offset of about 0.011 m along the –y axis.

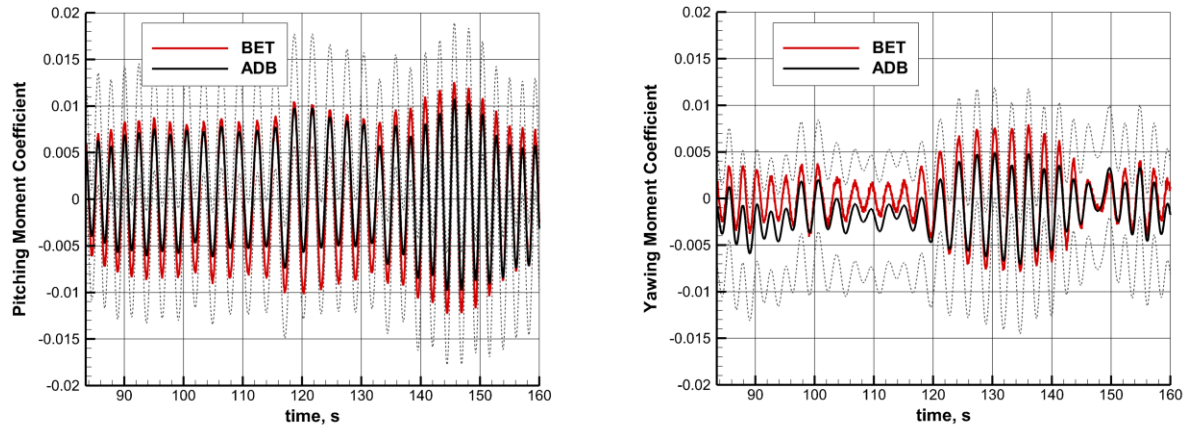

(a) (b)

Figure 23. a) Pitching moment coefficients, and b) yawing moment coefficients plotted against model values. Dashed lines denote model 3σ uncertainties.

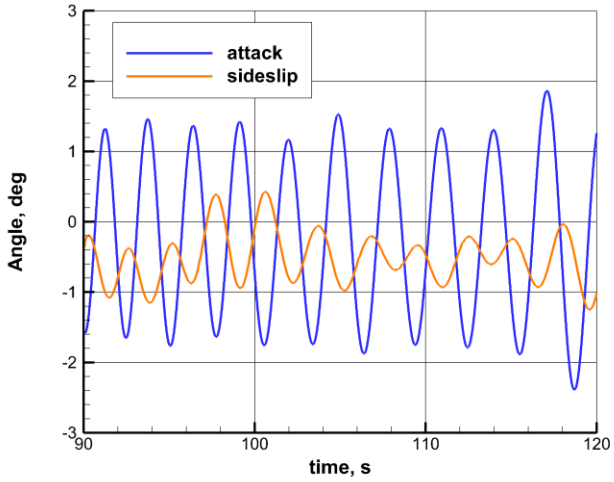

Figure 24. Sideslip trim angle of approximately -0.5° during SIAD cruise.

As detailed in Ref. 30, the mean pitch damping coefficient during SIAD cruise was estimated for a 10 s portion of the trajectory using a method based on the Euler-Cauchy (EC) equation[35]. The trajectory segment about the apex was used, as constant density is a limiting assumption of the EC method. As shown in Fig. 25(a), an analytical solution to the EC equation was fit to the reconstructed pitch rate data. The pitch damping coefficients extracted from each time step are plotted in Fig. 25(b) with the ADB model pitch damping curves. The data indicate that SIAD-R dynamic stability was greater than predicted, and extended to lower Mach numbers than tested in the ballistic range.

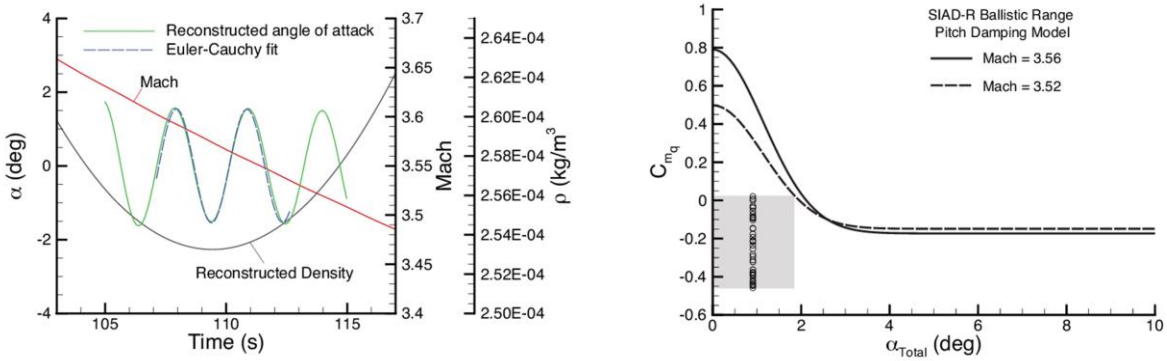

(a) (b)

Figure 25. a) Curve fit to reconstructed oscillation, Mach number, and density, and b) extracted C_{mq} points plotted with pitch damping model. From Ref. 31.

V. Post SFDT-1 Aerodynamic Model Changes

After SFDT-1 targeting, the aerodatabase was updated with model changes to the spin, despin, powered phase, and SIAD phase aerodynamic models. The spin and despin models were updated prior to flight but were not used in targeting activity due to time constraints. Updates to the powered phase and SIAD cruise models were motivated by comparisons to the reconstructed flight data.

Spin and despin model updates utilized the most accurate flight article geometry available, which had been refined to include plume deflectors, TPS, bridle covers, and other details. Additionally, spin-up freestream Mach number and angle of attack were updated to 0.01 and 163°, respectively, to reflect expected drop conditions. Pressure contours from the updated spin model solutions are shown in Fig. 26.

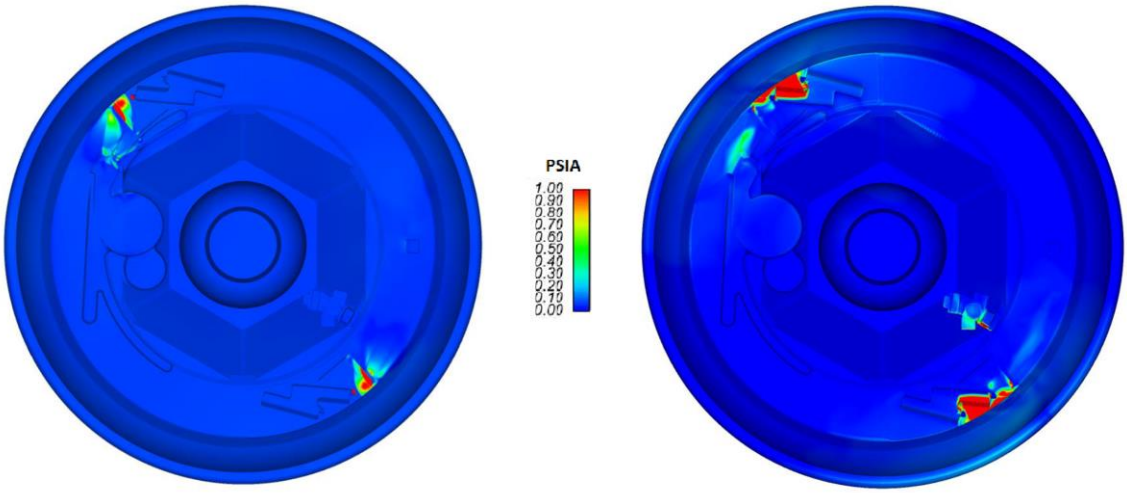

(a) (b)

Figure 26. Updated model computed aftbody pressure contours for spin motors 1&3 (a) and 2&4 (b).

As mentioned previously, the SFDT-1 reconstruction showed that the powered phase moment coefficient was overpredicted in the sub- and transonic regime, leading to underpredicted peak altitude in simulation. To better understand the cause of the model inaccuracy, CFD was run with high-fidelity TV geometry using the Loci-CHEM code at sub- and transonic conditions, both with and without the STAR-48 plume. The power-on moment coefficients thus obtained largely agreed with the flight reconstruction, and comparisons of predicted backshell pressure distributions with earlier computations confirmed that the powered phase aerodynamic moment was sensitive to the TV aft geometry at conditions below Mach 1.5. A correction to the ADB was implemented as a linear function of Mach<1.5 to reduce the powered phase moment coefficient magnitude there. The pre-flight model, reconstruction, and post-flight model total moment coefficient are plotted in Fig. 28(b). With no changes to other pre-flight models used in flight simulations, the powered phase correction increased the predicted peak altitude by 2.66 km. When combined with changes to other models (e.g., atmosphere, mass, thrust), flight simulations recreated the loft of SFDT-1 to within a few meters.

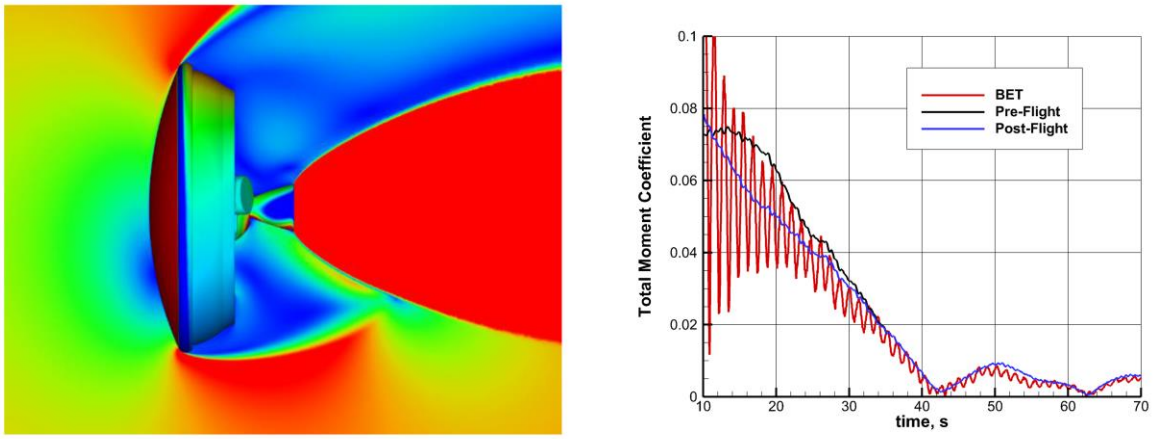

(a) (b)

Figure 28. a) Loci-CHEM subsonic powered phase solution; b) comparison of pre-flight, reconstructed, and post-flight powered phase total moment coefficient.

The final aerodynamic model adjustment motivated by SFDT-1 flight data was made to the SIAD phase, where the reconstruction indicated that the predicted pitching moment slope was shallow. The reason was found to be due to inadequate model angle of attack resolution, with the first nonzero point at 10°. Cases for each Mach table were run at 2° angle of attack, which increased the small angle pitching moment slope by 15.6% and reconciled the differences observed between the pre-flight model and flight reconstruction.

VI. Comparison of Improved Models to Reconstructed SFDT-2 Flight Data

The second flight of the LDSD test campaign, SFDT-2, was flown from PMRF on June 8, 2015. SFDT-2 lofted approximately 2.9 km higher than predicted, and experienced an unidentified disturbance shortly after despin which induced large angle of attack oscillations during subsequent coast and SIAD phases. The 30.5 m diameter supersonic ringsail (SSRS) parachute deployed successfully but failed at full inflation, however the flight disturbance was not directly implicated in its failure. SFDT-2 was reconstructed with the NewSTEP tool in much the same manner as SFDT-1. Because of previously mentioned difficulties in capturing impulsive events, analyses of the drop, spin-up, and despin phases are omitted from this section, and attention is focused on significant features of the powered, coast, and SIAD phases.

A. Powered Phase

The SFDT-2 powered phase plots are shown here for $t \geq 10$ s to avoid noisy data at the beginning of the burn. Smoothed BET side and normal force coefficients are plotted in Fig. 29(a), while moment coefficients are plotted in Fig. 29(b). Biases in the reconstructed coefficients are more pronounced than those of SFDT-1, again suggestive of a radial *cg* offset, thrust misalignment, or some combination thereof. A thrust misalignment angle of about 0.26° was calculated from normal force and thrust coefficients, approaching the 3σ thrust vector alignment uncertainty of 0.3°.

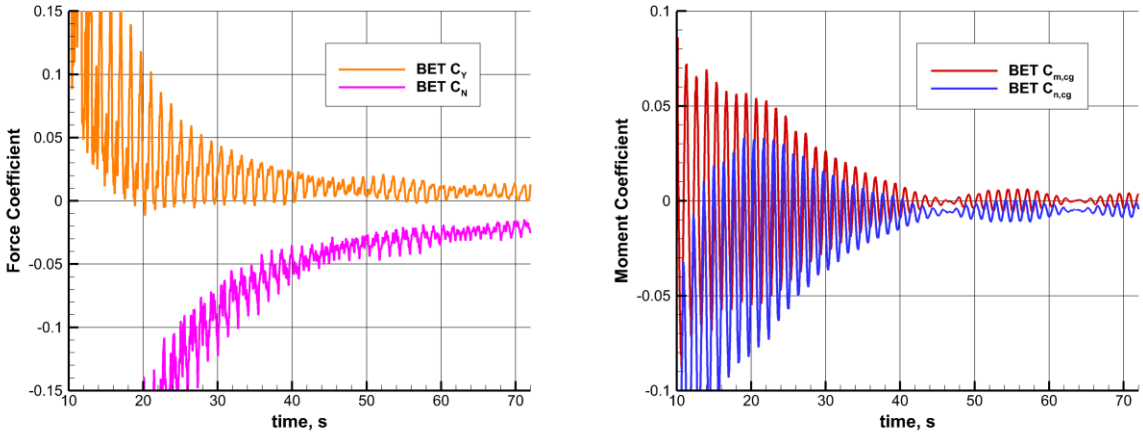

(a) (b)

Figure 29. Reconstructed a) side and normal force coefficients, and b) pitch and yaw moment coefficients.

BET and pre-flight ADB total moment coefficients for SFDT-1 and SFDT-2 powered phases over the range $0.1 \leq M_\infty \leq 1.5$ are plotted in Fig. 30. Informed by the SFDT-1 result, the SFDT-2 pre-flight model appears to track its flight data better, more closely following the mean about which the flight data oscillate due to wobbling and mass and/or thrust asymmetry. Oscillations in the model curves are the expected response of the axisymmetric model due to wobbling, which is of visibly greater amplitude in the second flight.

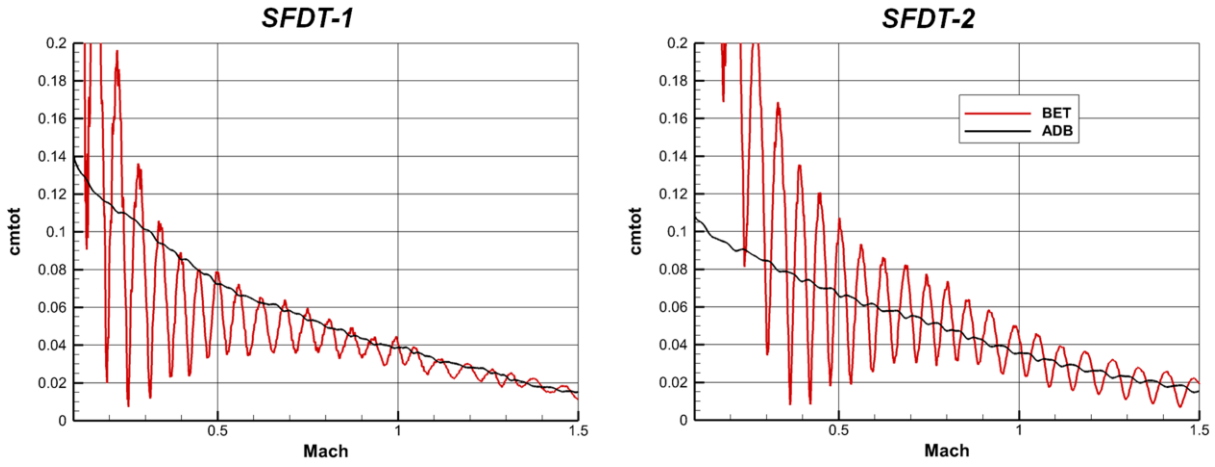

(a) (b)

Figure 30. Reconstructed and pre-flight predicted total moment coefficients: a) SFDT-1, b) SFDT-2.

B. Coast Phase

The SFDT-2 coast phase began at approximately *t*=72.5 s. Just after despin at about *t*=74.8 s, the SFDT-2 TV experienced an as-yet unexplained disturbance[37] which induced a sudden loss of drag, pitching motion, and subsequent angle of attack oscillations of up to nearly 30°. Reconstructed aerodynamic coefficients about the time of the disturbance are plotted in Fig. 31(a), and the aerodynamic angle history from late powered phase to ballute deploy conditions is plotted in Fig. 31(b). The angle of attack range of flight exceeded that of the ADB, so additional CFD cases up to 40° angle of attack were run for coast and SIAD phases with the same grids and codes as used previously. Where applicable, the results shown here were generated with the extended ADB.

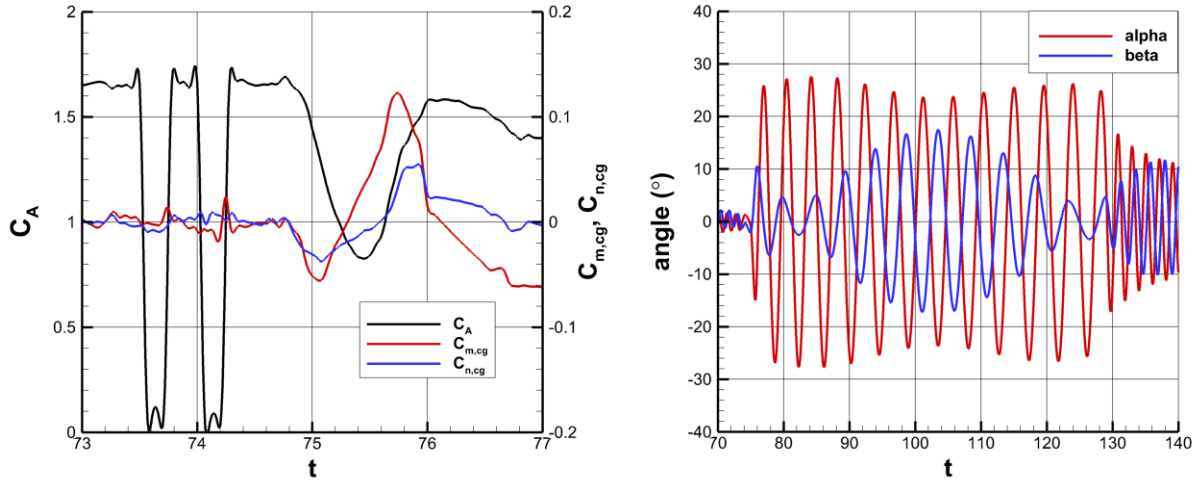

(a) (b)

Figure 31. a) Reconstructed aerodynamics around the time of the flight disturbance; b) TV aerodynamic angle history from end of powered phase to ballute deployment.

As shown in Fig. 31(a), reconstructed aerodynamics around the time of the disturbance appears to indicate the loss of nearly half the axial force over a period of about 1.2 s. The following high alpha oscillations compromised the expected TV drag performance, resulting in a longer than anticipated coast phase to decelerate to SIAD deployment at *t*=128.9 s. In spite of flying outside the anticipated angle of attack envelope, the post-disturbance coast phase was largely uneventful. The axial and normal force coefficient plots of Fig. 32 show that the predicted aerodynamic coefficients are in relatively good agreement with the flight data. Though well within model uncertainties, the moment coefficients appear to be slightly underpredicted, as shown in Fig. 33.

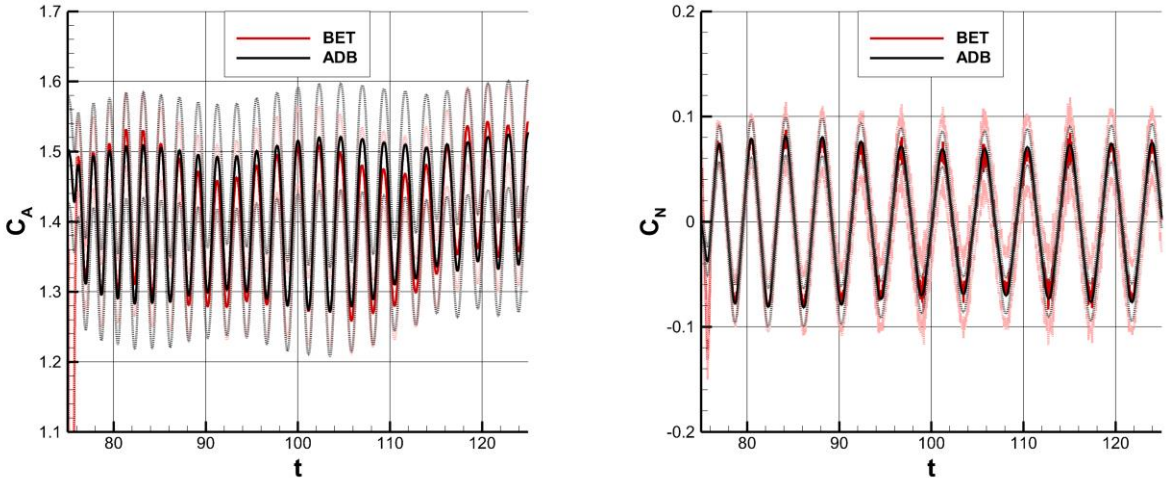

(a) (b)

Figure 32. SFDT-2 coast phase reconstructed and predicted: a) axial force coefficient; b) normal force coefficient.

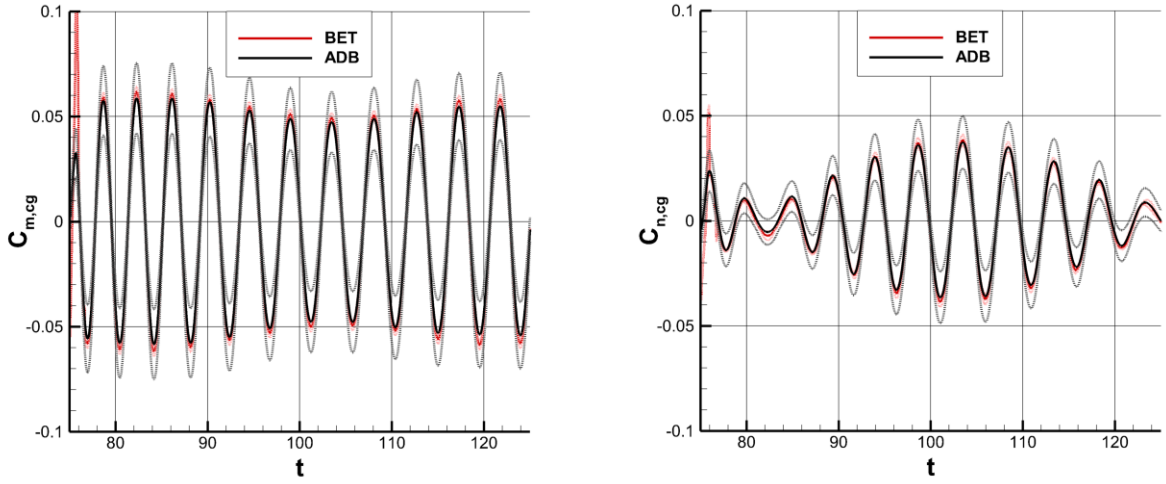

(a) (b)

Figure 33. SFDT-2 coast phase reconstructed and predicted: a) pitch moment coefficient; b) yaw moment coefficient.

C. SIAD Phase

Following a nominal SIAD deployment and inflation at t=128.9 s, the TV angle of attack oscillation amplitude was immediately reduced as shown in Fig. 31, owing to the increase in pitch stiffness realized with the deployed SIAD configuration. The plots in Figs. 34 and 35 below show comparisons between reconstructed and predicted force and moment coefficients over the interval $129.5 \leq t \leq 140.5$ s. As with the coast phase, the predicted aerodynamics match the flight data well, though the normal force and both moment coefficients appear to be slightly underpredicted.

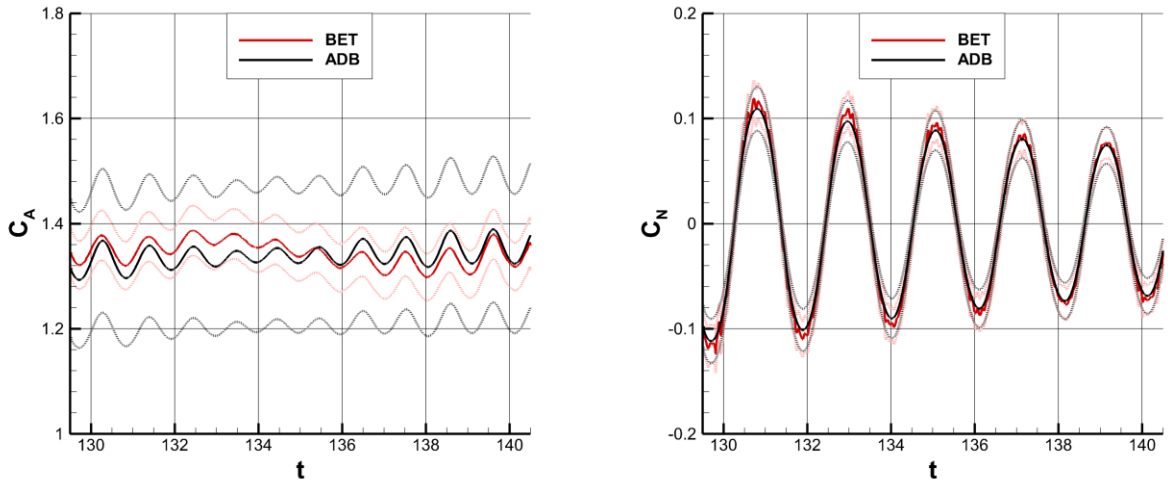

Figure 34. SFDT-2 SIAD phase reconstructed and predicted: a) axial force coefficient; b) normal force coefficient.

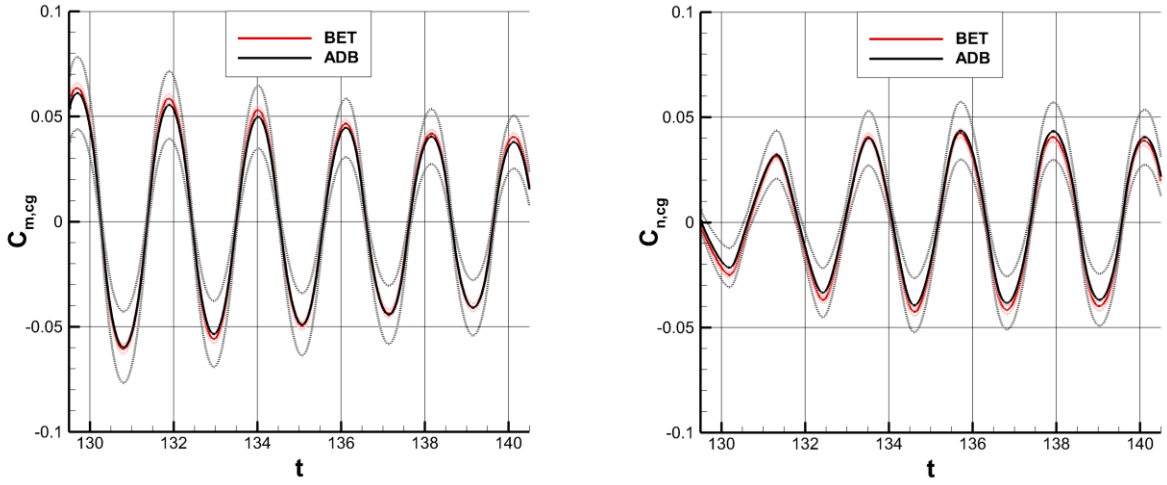

Figure 33. SFDT-2 SIAD phase reconstructed and predicted: a) pitch moment coefficient; b) yaw moment coefficient.

VII. Post-SFDT-2 Aerodynamic Model Changes

Using data from two flight tests, numerous flight simulations, and CFD results as a guide, the final aerodynamic database incorporated model changes where an improvement in simulation accuracy was thought to be obtainable. ADB adjustments made after SFDT-1 to reduce powered phase moment coefficient magnitudes were understood to be conservative, as there was reluctance within the program to introduce large model changes after a single test flight. The second flight, however, made clear that the powered phase model change needed to be expanded upon. As detailed in Ref. 38, the SFDT-2 trajectory reconciliation simulation run with the post-SFDT-1 model required that the moments carry relatively large uncertainty margins. The final modification to the powered phase model applied results from a series of powered phase CFD cases run with the Loci-CHEM solver at reconstructed SFDT-1 flight conditions. The aerodynamics of particular interest are shown in Fig. 34, where the new CFD runs indicated that a significant modification to the transonic axial force coefficient and a more subtle correction to the moment coefficient were in order. The new aerodynamics were implemented within the ADB by calculating scale factors between old and new coefficients, then applying the scale factors in simulation as a function of Mach number. The correction is applied up until Mach 1.5, where ADB and flight reconstructions were in good agreement. The modified, undispersed aerodatabase was tested in simulation and increased the trajectory peak altitude by 2.7 km, very close to the 2.9 km loft experienced in flight.

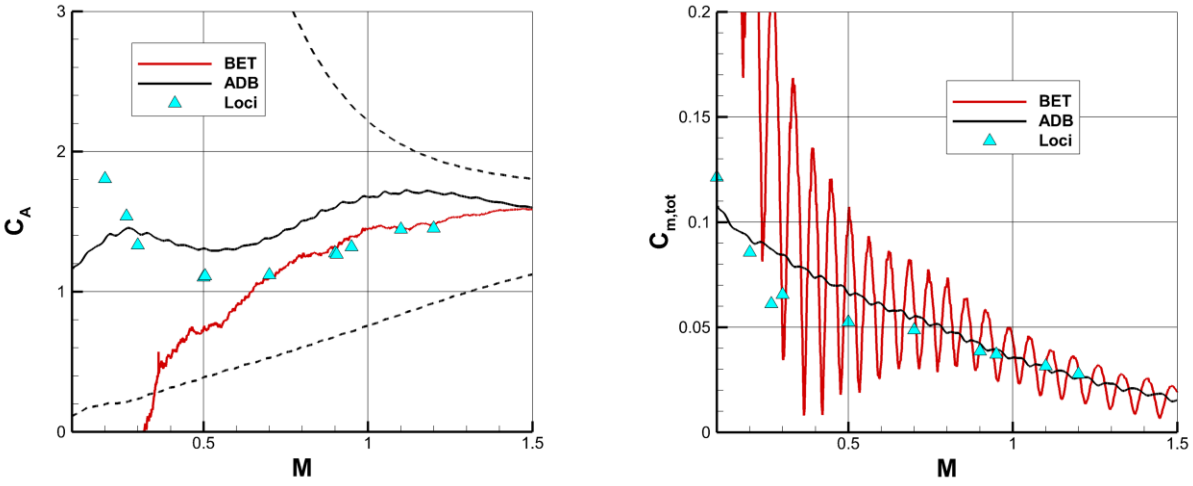

Figure 34. Comparison of SFDT-2 reconstruction, aerodatabase, and updated CFD results for a) axial force coefficient; b) total moment coefficient.

VIII. Conclusion

The Low Density Supersonic Decelerator (LDSD) program is designed to mature technologies that will enable high-mass Mars EDL operations. Supersonic Flight Dynamics Tests (SFDT) were conducted in 2014 and 2015 to demonstrate 6 meter robotic mission class supersonic inflatable aerodynamic decelerators (SIAD-R) and large supersonic parachutes. Aerodynamic models of the test vehicle (TV) were developed from historical data, physical approximations, and CFD, and are contained in an aerodatabase (ADB) code queried in flight simulations. The flight simulations are used to target test conditions and to reconcile observed differences between model predictions and flight. Models within the ADB include aerodynamics of the TV in drop, powered flight, coast, and SIAD flight phases, spin and despin motor plume interaction, and a SIAD inflation model.

After each SFDT flight, test vehicle aerodynamics were reconstructed from sensor data using the NewSTEP code and compared against the pre-flight aerodynamic models to assess model accuracy. The coast and SIAD phase

models performed satisfactorily, matching both reconstructed flights to well within model uncertainties. SFDT-1 reconstruction and simulation revealed that the trajectories were extremely sensitive to spin model accuracy, hence the respective ADB model was eventually obviated in simulation by matching reconstructed TV orientation and rates after spin-up. The despin and SIAD inflation disturbance models also fell out of use in later simulations, as flight reconstructions showed no evidence of off-nominal despin or SIAD deployment. The powered phase was identified as the most problematic of the ADB models after SFDT-1 lofted about 8 km higher than predicted. Post-flight analysis showed that over-predicted aerodynamic moments in the low-speed powered phase were a significant contributor to the loft. Corrections to reduce the ADB powered phase moment coefficient were implemented after each flight based upon reconstructed data and high-fidelity Loci-CHEM CFD simulations. In SFDT-2 reconciliation simulations, the final powered phase model increased peak altitude by 2.7 km, close to the 2.9 km loft of SFDT-2.

Acknowledgments

The authors are thankful for the work of other NASA Langley Research Center and Jet Propulsion Laboratory flight dynamics and flight reconstruction team members that contributed to the success of LDSD and SFDT, including (alphabetically) Seth Aaron, Eric Blood, Angela Bowes, Som Dutta, Jason Ginn, Mark Ivanov, Chris Karlgaard, Prasad Kutty, Clara O'Farrell, Dick Powell, Eric Queen, Bill Strauss, Scott Striepe, and Joseph White.

References

[1] Edquist, K.T., Korzun, A.M., Dyakonov, A.A., Studak, J.W., Kipp, D.M., and Dupzyk, I.C., "Development of Supersonic Retropropulsion for Future Mars Entry, Descent, and Landing Systems," Journal of Spacecraft and Rockets, Vol. 51, No. 3, May-June 2014.

[2] Hughes, S.J., Cheatwood, F.M., Dillman, R.A., Wright, H.S., DelCorso, J.A., and Calomino, A.M., "Hypersonic Inflatable Aerodynamic Decelerator (HIAD) Technology Development Overview," 21st AIAA Aerodynamic Decelerator Systems Technology Conference and Seminar, May 2011, Dublin.

[3] Clark, I.G., Adler, M., and Rivellini, T.P., "Development and Testing of a New Family of Supersonic Decelerators," AIAA Paper 2013-1252.

[4] Striepe, S.A., Powell, R.W., Desai, P.N., Queen, E.M., Way, D.W., Prince, J.L., Cianciolo, A.M., Davis, J.L., Litton, D.K., Maddock, R.M., Shidner, J.D., Winski, R.G., O'Keefe, S.A., Bowes, A.G., Aguirre, J.T., Garrison, C.A., Hoffman, J.A., Olds, A.D., Dutta, S., Zumwalt, C.H., White, J.P., Brauer, G.L., Marsh, S.M., "Program To Optimize Simulated Trajectories II (POST2): Utilization Manual," Vol. II, Version 3.0.NESC, 2014

[5] Balaram, J., Austin, R., Banerjee, P., Bentley, T., Henriquez, D., Martin, B., McMahon, E., and Sohl, G., "DSENDS - A High-Fidelity Dynamics and Spacecraft Simulator for Entry, Descent and Surface Landing," IEEE 2002 Aerospace Conference, Big Sky, Montana, March 9-16, 2002.

[6] Timmons, J.D., "Viking Balloon Launched Decelerator Test," 27th Congress International Astronautical Federation, Anaheim, October 1976.

[7] Moog, R.D., Bendura, R.J., Timmons, J.D., and Lau, R.A., "Qualification Flight Tests of the Viking Decelerator System," AIAA Paper 73-457, May 1973.

[8] B.T. Cook, G. Blando, A. Kennett, M. Von Der Heydt, J.L. Wolff, and M. Yerdon, "High Altitude Supersonic Decelerator Test Vehicle," AIAA Aerodynamic Declerator Systems Conference, March 2013, Daytona.

[9] Clark, I.G., Adler, M., and Rivellini, T.P., "Development and Testing of a New Family of Supersonic Decelerators," AIAA Paper 2013-1252.

[10] http://fun3d.larc.nasa.gov

[11] Nichols, R.H., and Buning, P.G., "User's Manual for OVERFLOW 2.2," Version 2.2, August 2010.

[12] Wright, M.J., White, T.R., and Mangini, N., "Data Parallel Line Relaxation (DPLR) Code User Manual: Acadia, Version 4.01.1," NASA TM 2009-215388, 2009.

[12] Luke, E. A., Tong, X-L., Wu, J., Tang, L., and Cinnella, P., "CHEM: A Chemically Reacting Flow Solver for Generalized Grids," AIAA 2003.

[14] Yates, L., "Aerodynamic Coefficients from Aeroballistic Range Testing of Deployed and Stowed-SIAD SFDT Models," Final Report, May 22, 2012.

[15] Schoenenberger, M., Dyakonov, A., and Van Norman, J., "Mars Science Laboratory Aerodynamic Database Release 1.0," NASA Langley Research Center, May 2012.

[16] Samareh, J., "GridTool: A Surface Modeling and Grid Generation Tool," Proceedings of the Workshop on Surface Modeling, Grid Generation, and Related Issues in CFD Solutions, NASA CP-3291, May 9-11, 1995.
[17] Pirzadeh, S., "Viscous Unstructured Three-Dimensional Grids by the Advancing-Layers Method," AIAA 94-0417, January 1994.
[18] Schoenenberger, M., Van Norman, J., Rhode, M., and Paulson, J., "Characterization of Aerodynamic Interactions with the Mars Science Laboratory Reaction Control System Using Computation and Experiment," 51st AIAA Aerospace Sciences Meeting, Grapevine, January 2013.
[19] Dyakonov, A.A., Glass, C.E., Desai, P.N., and Van Norman, J.W., "Analysis of Effectiveness of Phoenix Entry Reaction Control System," Journal of Spacecraft and Rockets, Vol. 48, No. 5, September-October 2011.
[20] Smith, S.D., "High Altitude Supersonic Flow of Chemically Reacting Gas-Particle Mixtures – Volume 1 – A Theoretical Analysis and Development of the Numerical Solution," LMSC HREC TM D390409, Lockheed Missiles & Space Company, Huntsville, AL, October 1974.
[21] Evans, R.M., "Boundary Layer Integral Matrix Procedure BLIMPJ User's Manual," UN-75-64 Aerotherm, Mountain View, CA, July 1975.
[22] Marcum, D.L., "Adaptive Unstructured Grid Generation for Viscous Flow Applications," AIAA Journal, Vol. 34, No. 11, p. 2440, 1996.
[23] Alliant Techsystems, Inc., "ATK Space Propulsion Products Catalog," August 2012.
[24] CAP Aerodynamics, "Orion Aerodynamics Databook Version 0.53," NASA CXP-72167, May 2009.
[25] Roberts, B.B., Wallace, R.O., Craig, M.K, and Kanipe, D.B., "Rocket Exhaust Plume Induced Flowfield Interaction Experiences with the Space Shuttle," AIAA 18th Thermophysics Conference, Montreal, 1983.
[26] Bohon, H.L. and Miserentino, R., "Deployment and Performance Characteristics of 5-Foot-Diameter Attached Inflatable Decelerators From Mach Number 2.2 to 4.4," NASA TN D-5840, August 1970.
[27] Giersch, L., Rivellini, T., Clark, I., Shook, L., Ware, J., and Welch, J., "SIAD-R: A Supersonic Inflatable Decelerator for Robotic Missions to Mars," AIAA Aerodynamic Decelerator Systems Conference, Daytona, March 2013.
[28] Muppidi, S., Tang, C., Van Norman, J.W., Bose, D., Clark, I., and Coatta, D., "Aerodynamic Analysis of Next Generation Supersonic Decelerators," 32nd AIAA Applied Aerodynamics Conference, Atlanta, June 2014.
[29] Tang, C., Muppidi, S., Van Norman, J.W., Tanimoto, R., Bose, D., and Clark, I., "Aerodynamic and Aerothermal Analysis of the Supersonic Inflatable Aerodynamic Decelerator-Robotic (SIAD-R)," 23rd AIAA Aerodynamic Decelerator Systems Technology Conference and Seminar, Daytona, March-April 2015.
[30] Kutty, P., Karlgaard, C.D., Blood, E.M., O'Farrell, C., Ginn, J.M., Schoenenberger, M., and Dutta, S., "Supersonic Flight Dynamics Test: Trajectory, Atmosphere, and Aerodynamics Reconstruction," AAS 15-224.
[31] Karlgaard, C.D., Tartabini, P.V., Blanchard, R.C., Kirsch, M., and Toniolo, M.D., "Hyper-X Post-Flight Trajectory Reconstruction," Journal of Spacecraft and Rockets, Vol. 43, No. 1, 2006, pp. 105-115.
[32] Karlgaard, C.D., Beck, R.E., Derry, S.D., Brandon, J.M., Starr, B.R., Tartabini, P.V., and Olds, A.D., "Ares I-X Trajectory Reconstruction: Methodology and Results," Journal of Spacecraft and Rockets, Vol. 50, No. 3, 2013, pp. 641–661.
[33] Schoenenberger, M., Van Norman, J., Karlgaard, C.D., Kutty, P., and Way, D., "Assessment of the Reconstructed Aerodynamics of the Mars Science Laboratory Entry Vehicle," Journal of Spacecraft and Rockets, Vol. 51, No. 4, 2014, pp. 1076-1093.
[34] Dutta, S., Bowes, A.L., Striepe, S.A., Davis, J.L., Queen, E.M., Blood, E.M., and Ivanov, M.C., "Supersonic Flight Dynamics Test 1 – Post-Flight Assessment of Simulation Performance," 25th AAS/AIAA Space Flight Mechanics Meeting, Willaimsburg, Virginia, January-February 2015.
[35] Schoenenberger, M., Queen, E. M., and Litton, D., "Oscillation Amplitude Growth for a Decelerating Object with Constant Pitch Damping," AIAA 2006–6148, 2006.
[36] Queen, E., Bowes, A., Dutta, S., Van Norman, J., Way, D., and White, J., "Anomalous Accelerations During SFDT-2 Test Flight," NASA Langley Research Center, 2016.
[37] Dutta, S., Bowes, A.L., White, J.P., Striepe, S.A., Queen, E.M., O'Farrell, C., and Ivanov, M.C., "Post-Flight Assessment of Low Density Supersonic Decelerator Flight Dynamics Test 2 Simulation," AAS 16-222, AAS/AIAA Space Flight Mechanics Meeting, Napa, CA, 2016.